
MoR: MIXTURE OF REPRESENTATIONS FOR MIXED-PRECISION TRAINING

A PREPRINT

Bor-Yiing Su
Nvidia

boryiings@nvidia.com

Peter Dykas
Nvidia

wdykas@nvidia.com

Mike Chrzanowski
Nvidia

mchrzanowski@nvidia.com

Jatin Chhugani *

Meta

jatinch@meta.com

ABSTRACT

Mixed-precision training is a crucial technique for scaling deep learning models, but successful mixed-precision training requires identifying and applying the right combination of training methods. This paper presents our preliminary study on Mixture-of-Representations (MoR), a novel, per-tensor and sub-tensor level quantization framework that dynamically analyzes a tensor’s numerical properties to select between a variety of different representations. Based on the framework, we have proposed and experimented concrete algorithms that choose dynamically between FP8 and BF16 representations for both per-tensor and sub-tensor level granularities. Our universal approach is designed to preserve model quality across various quantization partition strategies and datasets. Our initial findings show that this approach can achieve state-of-the-art results with 98.38% of tensors quantized to the FP8 format. This work highlights the potential of dynamic, property-aware quantization while preserving model quality. We believe this approach can generally improve the robustness of low precision training, as demonstrated by achieving FP8 accuracies that are on par with existing approaches without the need for fine-grain partitioning, or can be used in combination with other training methods to improve the leverage of even lower precision number formats such as NVFP4.

1 Introduction

The scaling law [1] suggests that model performance increases with the number of parameters and the volume of training data, fueling a race to train ever-larger foundation models to achieve state-of-the-art performance on industry benchmarks. For instance, the Llama 3.1 405B model was trained on 24,576 H100 GPUs for months [2], the Megatron-Turing NLG 530B model on 4,480 GPUs for months [3], the GPT-4 model was estimated to have been trained on over 20,000 GPUs for three months [4], and the DeepSeek-V3 671B model is trained with 2.788M GPU hours [5]. Consequently, training large foundation models is time-consuming, power-hungry, and expensive. This has led to significant investment in optimizing the training workflow to accelerate performance and reduce resource consumption. Among the most effective optimizations is the use of low-precision numerical representations.

Using low-precision representations offers numerous benefits: (a) From a compute perspective, modern hardware offers significant speedups for lower-precision numerical operations. For example, an NVIDIA H100 GPU delivers 2x the FLOPS for FP8 GEMM operations compared to BF16 [6], while the newer GB200 and GU300 GPUs provide 4x and 6x FLOPS for FP4 GEMM, respectively [7, 8]. (b) From a bandwidth perspective, loading a vector of FP8 values requires only half the memory bandwidth of loading a BF16 vector of the same length. Therefore, low-precision representations directly reduce the latency of both computation and memory access, significantly accelerating training. (c) Moreover, applying low-precision formats during training enables their direct use for inference, creating consistency between the two phases and obviating the need for post-training quantization (PTQ) or quantization-aware training (QAT).

The formal specification of the FP8 format can be found in [9]. It defines two FP8 formats: E4M3 and E5M2. The E4M3 format has 4 bits for exponent, and 3 bits for mantissa; while the E5M2 format has 5 bits for exponent, and 2 bits for mantissa. But FP8 training is not only about the FP8 formats. In order to increase the representation accuracy, improve the training stability, and also retain the model quality, many prior arts define comprehensive recipes for FP8

*Work done while at Nvidia.

training. [10] and [9] suggested current and delayed per-tensor scaling. Essentially, defining a scaling factor for the full tensor to shift the numerical range of the tensor to the representable range by the format type. Delayed scaling computes this scaling factor based on historical absolute maximum (amax) values of the tensor; while current scaling computes this scaling factor based on the amax of the current tensor. [11] suggested partitioning the tensor into blocks, and compute one scaling factor per block. Llama3 [2] uses per-channel scaling that computes one scaling factor per row or column based on the dot product direction. DeepSeekV3 [5] combines both sub-channel scaling and per-block scaling into the recipe, and proposes using 1×128 sub-channel scaling for the activation tensor, and 128×128 per-block scaling for the weight tensor to achieve a balance between fine grained control and computational overhead. The micro-scaling format [12, 13, 14] suggested using a fine-grained 1×32 sub-channel block to compute the scaling factor. The NVFP4 format [15] suggested using a fine-grained 1×16 sub-channel block to compute the scaling factor.

Another common strategy is to selectively apply FP8 quantization. [16, 9] used E4M3 format in the forward pass, and uses E5M2 format in the backward pass. [17] used per-group scaling for the optimizer states, and per-tensor scaling for the activation tensors. [18] suggested using fp4 format for the majority of the training, but fall back to higher precision (FP32/BF16) at the late stage of training. [19] applied nvfp4 for most of the layers, but left the first two and last eight layers in BF16, it also studied how reducing the number of BF16 layers affect model quality.

All of these prior arts focus on selecting the right methods and determining their appropriate application point (location and time) to create a low-precision training recipe that preserves model quality. What we are trying to accomplish, however, is to start gaining insights into why a specific recipe can achieve model quality on par with the baseline. Therefore, we developed the MoR framework, which attempts to capture invariance through tensor analysis. In this paper, we also showed that relative error can serve as a reasonable invariance for FP8 training. While works like DeepSeekV3 [5] and MXFP8 [14] achieve good results because their fine-grained partition ensures that the quantization error is small for all tensors, we illustrated that using relative error as an invariance allows us to obtain on-par model quality with much coarser-grained partitions. The relative error invariance we use is conservative and serves as a sufficient, but not a necessary, condition. We plan to continue working in this direction to explore invariance metrics that are more efficient and can be used for more aggressive quantization formats (such as NVFP4).

Our primary contributions are as follows:

1. We propose a new strategy for computing the scaling factor that ensures consistency across the entire tensor, regardless of the chosen scaling granularity.
2. We introduce a novel dynamic quantization framework that makes real-time decisions based on numerical properties at runtime, allowing the model to adapt precision throughout the training process.
3. Using this framework, we develop and evaluate tensor-level and sub-tensor-level **Mixture-of-Representations (MoR)** recipes that dynamically select FP8 and BF16 types, achieving substantial efficiency without compromising quality.

2 Group Amax Mantissa Scaling

A major challenge for low-precision quantization is that it requires mapping a tensor’s wide dynamic range to the limited representable range of the target format, such as FP8. For example, the E4M3 FP8 format can only represent positive values between 2^{-9} and 448; and the E5M2 FP8 format can only represent positive values between 2^{-16} and 57,344. Quantizing values outside this range leads to information loss through either **saturation** (clipping large values) or **underflow** (flushing small values to zero). An effective strategy is to compute a scaling factor that shifts the tensor’s values into the representable range, minimizing these quantization errors and preserving numerical fidelity.

The prevailing hypothesis in quantization is that large-magnitude values are more critical to preserve than small ones. Consequently, the standard scaling strategy, used in all prior arts [9, 10, 17, 11, 2, 5, 13], is to compute a scaling factor that maps the absolute maximum value (amax) of a tensor to the maximum representable value of the quantization format. This prioritizes avoiding saturation at the cost of flushing smaller values to zero.

Beyond the strategy, the numerical format of the scaling factor itself introduces a critical trade-off. Using a high-precision format like FP32 preserves the amax value the best but adds significant metadata overhead. To reduce this cost, prior work has explored lower-precision formats. The micro-scaling format [13] uses E8M0, which offers a wide dynamic range for the scaling factor, while NVFP4 [15] suggests E4M3, which represents the amax with higher accuracy but has a more limited range. These approaches present a fundamental conflict: one must choose between the wider **range** of E8M0 and the higher **precision** of E4M3, or falling back to FP32 with higher memory cost.

To resolve this trade-off, we propose the **Group Amax Mantissa (GAM) scaling algorithm**. The goal of GAM is to combine the respective strengths of prior approaches: to design a scaling factor representation that achieves the

Algorithm 1: Group Amax Mantissa Scaling

Input: A tensor \mathbf{X} ; a partition $G = \{g_i\}$ over the elements of \mathbf{X} ; for each group $g \in G$, a partition $B_g = \{b_j\}$ of g into blocks, quantization type amax q_{amax}

Output: The union of all group mantissas M and all block scale factors in E8M0 S

```

foreach group  $g$  in  $G$  do
   $g_{amax} \leftarrow \max(\text{abs}(g))$ ;
   $s_g \leftarrow q_{amax}/g_{amax}$ ;
   $m_g \leftarrow \text{mantissa}(s_g)$ ;
  foreach block  $b$  in  $B_g$  do
     $b_{amax} \leftarrow \max(\text{abs}(b))$ ;
     $s_b \leftarrow q_{amax}/b_{amax}$ ;
     $m_b \leftarrow \text{mantissa}(s_b)$ ;
    /* Preventing saturation from happening by rounding down the exponent when
        $m_g > m_b$ 
    if  $m_g \leq m_b$  then
       $s_b \leftarrow \text{exponent}(s_b)$ ;
    else
       $s_b \leftarrow \text{exponent}(s_b) - 1$ ;
    
```

return $M \leftarrow \bigcup_{g \in G} \{m_g\}$, $S \leftarrow \bigcup_{b \in B} \{s_b\}$

wide dynamic range of an E8M0-like exponent while preserving the tensor’s maximum value with the high precision characteristic of an FP32 mantissa.

The core idea of GAM, detailed in Algorithm 1, is to decouple the mantissa and exponent of the scaling factors. We partition a tensor \mathbf{X} into blocks b , which are organized into groups g . For each group, we find the group-level amax (g_{amax}) and compute an ideal FP32 scaling factor s_g . We then store only the mantissa (m_g) of this group-level scaling factor. Subsequently, for each block b within that group, we compute its local amax (b_{amax}) and its corresponding ideal FP32 scaling factor s_b . From s_b , we extract only the exponent. A crucial rounding step adjusts this block exponent downward if the block’s mantissa (m_b) is smaller than the group’s shared mantissa (m_g). This is to prevent saturation from happening. To apply scaling, the per-block FP32 scaling factor is reconstructed on-the-fly by combining the shared 23-bit group mantissa m_g with the stored 8-bit per-block exponent.

While the group concept is generic, there is a trade-off between overhead and quantization error. Smaller groups will have more overhead but with smaller quantization error, while larger groups will have less overhead but with larger quantization error. In our experiments, we use a single group for the entire tensor, which is sufficient for the FP8 format as shown in our experiments in Section 4.1. This configuration offers three primary benefits:

1. **Negligible Overhead:** The storage cost is minimal. Each block requires an 8-bit exponent, and the entire tensor only needs one additional 23-bit mantissa.
2. **Maximum Precision:** The absolute maximum value of the entire tensor is used to derive the mantissa, preserving it with full FP32 precision.
3. **Consistent Mantissa Operations:** During scaling or de-scaling steps, the mantissa component of the reconstructed scaling factor is identical for all values. This makes the mantissa operations orthogonal to the block sizes. On the other hand, the exponent value of the scaling factor still depends on the block size and is subject to change based on the block amax value.

3 The MoR Framework

The Mixture-of-Representations (MoR) framework, outlined in Algorithm 2, provides a systematic approach for dynamically selecting quantization strategies. Given an input tensor, the framework first partitions it into a set of blocks B according to a chosen quantization granularity. For per-tensor quantization, B contains a single block (the entire tensor); for 2D block quantization, B is the set of all 2D blocks; for per-channel quantization, B consists of the corresponding rows or columns based on the dot product dimension; for sub-channel quantization, B is the union of all sub-channel sub-rows or sub-columns.

Algorithm 2: MoR Framework

Input: A tensor \mathbf{X} ; a partition $B = \{b_i\}$ of \mathbf{X} into blocks; an ordered list of tensor representation types T_1 to T_k ; an ordered list of criteria metrics M_1 to M_{k-1} ; additional metadata A required to perform quantization

Output: The quantized tensor \mathbf{X}_Q and all block quantization metadata D

```

foreach block  $b$  in  $B$  do
  for  $i \leftarrow 1$  to  $k$  do
    if  $i = k$  then
       $b_Q, d_b \leftarrow$  Quantize block  $b$  to type  $T_k$ ;
      break;
    if  $M_i(B, b, A)$  then
       $b_Q, d_b \leftarrow$  Quantize block  $b$  to type  $T_i$ ;
      break;
  return  $\mathbf{X}_Q \leftarrow \bigcup_{b \in B} \{b_Q\}$ ,  $D \leftarrow \bigcup_{b \in B} \{d_b\}$ 

```

The framework operates by iterating through an ordered list of target quantization types, ranked from **most aggressive** (e.g. E4M3) to **least aggressive** (e.g. BF16). For each block, the goal is to successfully apply the most preferred low-precision format. A set of predefined metrics determines whether a given quantization type is acceptable for the block. If the acceptance criteria for the current type are met, the block is quantized using that type, and the process concludes for that block. If the criteria are not met, the framework falls back to the next type in the list. In the [E4M3, E5M2, BF16] example, if the metric for E4M3 returns false, the framework then evaluates E5M2. If E5M2 also fails, it falls back to BF16, effectively leaving the block in its original precision. When using the GAM scaling algorithm from Section 2, the additional metadata A in the algorithm refers to the group mantissa M , which can be used in the metrics evaluations. The block quantization metadata D refers to the E8M0 block scaling factor S , which is one of the output values when quantizing the block.

This approach is similar to the one presented in the FGMP paper [20], which uses per-channel quantization and independently quantizes each row or column into FP4 or FP8 based on metrics such as quantization error, estimated matrix multiplication error, or block sensitivity.

Building on our MoR framework, we developed and evaluated two distinct mixed-precision recipes: tensor-level MoR and sub-tensor-level MoR, which are detailed in the following sections.

3.1 MoR at Tensor Granularity

In tensor-level MoR, a single quantization type is selected for an entire tensor, though different tensors within a model can be quantized to different types. Take Figure 1 as an example, layer #1 is the linear projection module, layer #2 is the attention module, layer #3 is the out projection module, layer #4 is the layer norm module, layer #5 is the MLP module, and layer #6 is the layer norm module. Suppose we want to quantize the MLP module #5, the tensors could be treated differently: the weight tensors M_1, M_2 , and the activation tensor Z_1 might be quantized to E4M3, while the activation tensor F remains in BF16.

We implemented and evaluated a specific tensor-level MoR recipe based on our framework (Algorithm 2). In this recipe, the ordered list of representation types is [E4M3, BF16]. The acceptance metric for E4M3 is that the tensor's mean relative quantization error, calculated over all non-zero elements, must be less than a threshold th_{E4M3} :

$$n \leftarrow \sum_{x_{i,j} \in X, x_{i,j} \neq 0} 1 \quad (1)$$

$$\text{error} = \frac{1}{n} \sum_{x_{i,j} \in X, x_{i,j} \neq 0} \left| \frac{x_{i,j} - Q(x_{i,j})}{x_{i,j}} \right| < th_{E4M3} \quad (2)$$

where n is the count of non-zero elements in tensor X , and Q is the function that quantizes an element from its original format (e.g., BF16) to E4M3. If the computed error exceeds the threshold, the E4M3 quantization is rejected, and the entire tensor reverts to BF16.

A key aspect of this approach is that while the final decision (E4M3 or BF16) is global to the tensor, the underlying quantization and error calculation can leverage different partitioning strategies. Figure 2 illustrates this idea. We first computes the global absolute maximum value to retrieve the global mantissa M using the GAM scaling algorithm

(Algorithm 1). Then we quantize the tensor into E4M3 with different partition strategies. We partition the tensor into 128×128 blocks, keep the full tensor non-partitioned, or partition the tensor based on the dot product channel. The purple squares in the figure represent the E8M0 scaling factors that are required for different partitioning strategies. We compute the local quantization error using the relative error metric for each block b based on the partitioning strategy, and then aggregate the local errors into the global quantization error. This global error is then compared against the threshold to make the final, tensor-wide decision. The primary advantage of this approach is to isolate model quality considerations from representation efficiency considerations. The hypothesis is in the following: as long as the relative error of the representation is bounded, we can guarantee the model quality to be on par compared to the BF16 baseline. So we are free to explore different partitioning strategies to further improve the representation efficiency as long as the relative error bound condition is met.

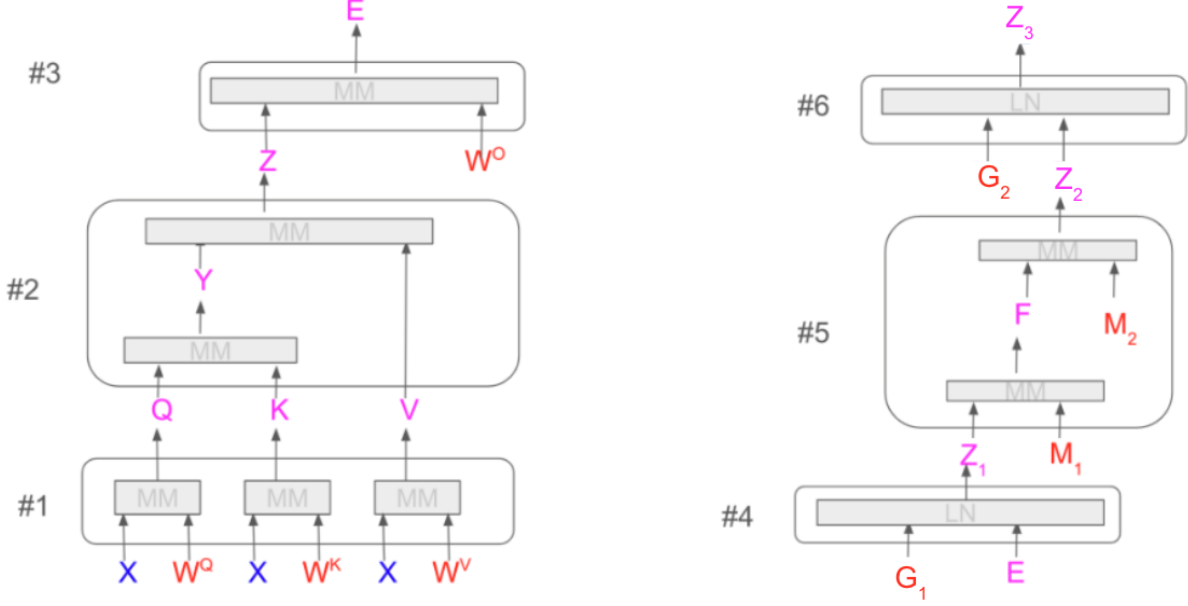


Figure 1: A diagram of the Transformer block architecture.

3.2 MoR at SubTensor Granularity

MoR at sub-tensor granularity means we can apply different quantization types to different partition blocks. Figure 3 illustrates such concept. The yellow blocks are quantized to the E4M3 type; the blue blocks are quantized to E5M2 type; and the green blocks are not quantized and stay at the original BF16 type (assuming the original input tensor type is BF16). The GEMM operation is much more complicated in this case, as we might need to perform GEMM on blocks with different types. If there is no hardware support to perform the dot product of two different tensor types, we will upcast the quantized block to match the operand with higher precision. For example, in Figure 3, A_{13} is in BF16, while B_{31} is in E4M3, if there is no hardware support for such dot product, we will upcast B_{31} to BF16 and perform BF16 GEMM between the two blocks.

Sub-tensor MoR applies the framework’s decision logic at the block level, allowing different blocks within the same tensor to have different quantization types. This concept is illustrated in Figure 3, where a single tensor is composed of blocks in E4M3 (yellow), E5M2 (blue), and the original BF16 format (green). The GEMM operation is much more complicated in this case, as we might need to perform GEMM on blocks with different types. If there is no hardware support to perform the dot product of two different tensor types, we will upcast the quantized block to match the operand with higher precision. For example, in Figure 3, A_{13} is in BF16, while B_{31} is in E4M3, if there is no hardware support for such dot product, we will upcast B_{31} to BF16 and perform BF16 GEMM between the two blocks.

We developed and evaluated two sub-tensor MoR recipes based on our framework (Algorithm 2).

Algorithm 1: Three-Way Selection (E4M3/E5M2/BF16) The first algorithm uses an ordered list of types [E4M3, E5M2, BF16]. The decision process for a block b is as follows:

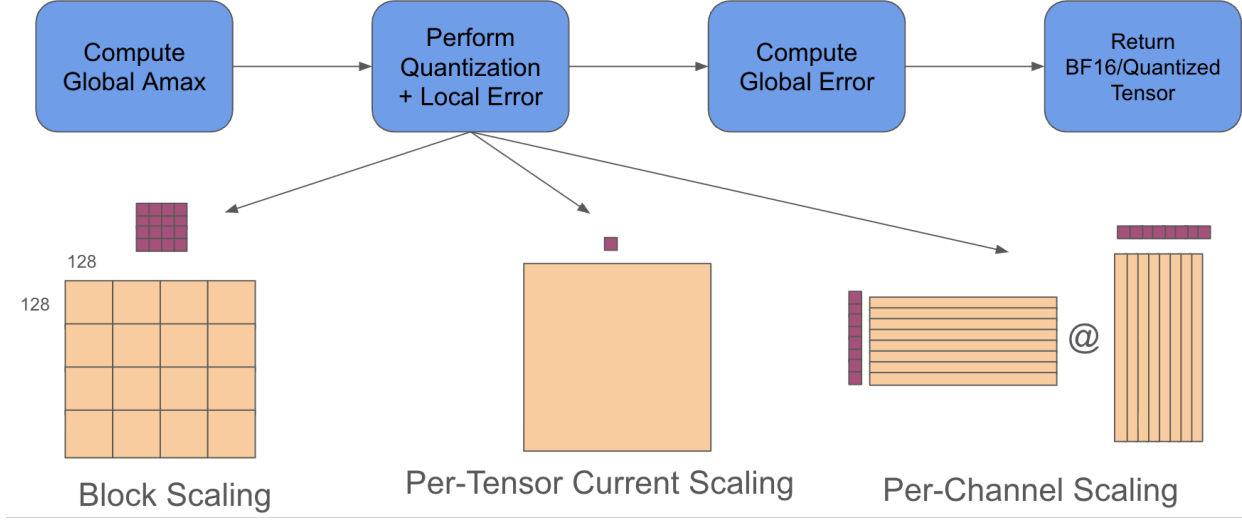


Figure 2: Illustration of tensor-level MoR. A single decision (E4M3 or BF16) is made for the entire tensor X . This decision is based on a global relative error, which can be computed using various internal partitioning strategies for the quantization step (e.g., per-block, no-partition, per-channel). The process uses the GAM scaling algorithm from Algorithm 1 to determine a shared mantissa and per-partition exponents (purple squares).

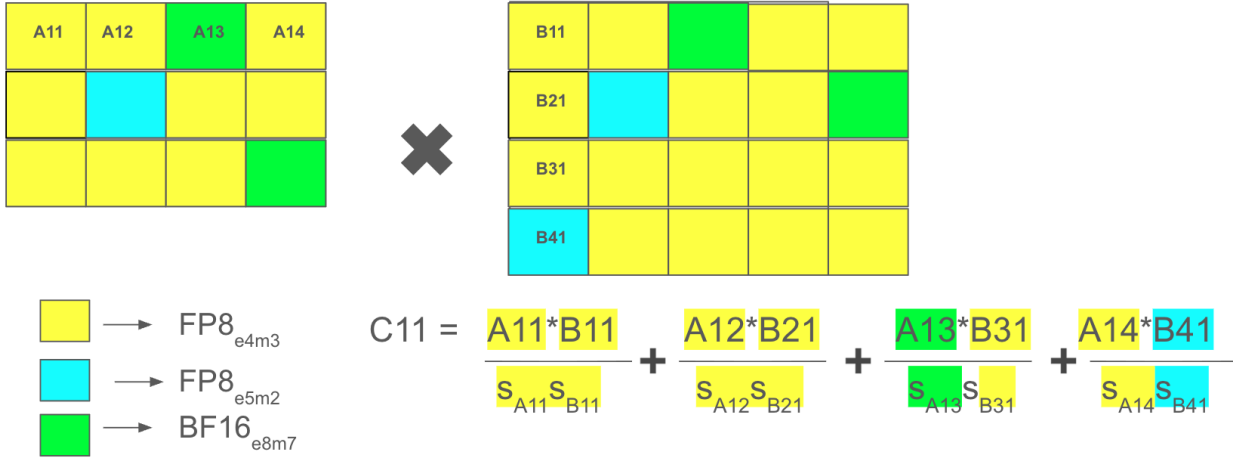


Figure 3: An illustration of sub-tensor MoR. Blocks within matrices A and B are quantized to different formats (E4M3, E5M2, BF16). The corresponding GEMM operation may require upcasting blocks (e.g., B_{31}) to a higher precision (BF16) before multiplication.

1. **Check E4M3:** The block is quantized to E4M3 if its total relative error is lower than if it were quantized to E5M2. This is the metric M_1 :

$$\sum_{x \in b, x \neq 0} \left| \frac{x - Q_{E4M3}(x)}{x} \right| < \sum_{x \in b, x \neq 0} \left| \frac{x - Q_{E5M2}(x)}{x} \right| \quad (3)$$

2. **Check E5M2:** If the E4M3 check fails, the framework then checks if the block’s dynamic range fits within the representable normal range of E5M2 (the maximum value representable by the E5M2 type is 57344, and the smallest value in the normal range of the E5M2 type is 2^{-14}). This is the metric M_2 :

$$\frac{\max(\text{abs}(b))}{\min(\text{abs}(b))} < \frac{57344}{2^{-14}} \quad (4)$$

3. **Fallback:** If both checks fail, the block remains in BF16.

Algorithm 2: Two-Way Selection (E4M3/BF16) The second algorithm is a simpler variation that uses the ordered list [E4M3, BF16]. It uses the exact same metric as in Equation 3 to evaluate E4M3. However, the logic is different: if E4M3 quantization yields a higher relative error than E5M2, the framework does not consider E5M2 as an alternative. Instead, it immediately falls back to BF16. In this recipe, E5M2 serves only as a high-quality benchmark to determine if E4M3 is a suitable choice, but it is never selected as the final format.

4 Experiments

All experiments were performed on the Nemotron-3 8B model [21], a dense transformer model with 32 transformer blocks. Our quantization strategy targets only the linear layers within each transformer block. Specifically, we apply the MoR algorithms to four linear layers in one transformer block. For each linear layer, we apply MoR on the activation, weight, and gradient tensors and their transposes for the forward and backward pass GEMM operations. Using Figure 1 as an illustration, we apply MoR on layer #1: Linear QKV, this layer projects the input tensor to the Q, K, and V space; layer #3, Linear Projection, this layer projects the attention output to an output dimension; layer #5, FC1 and FC2, these are the two fully connected layers in the MLP module. All models were trained using the Megatron-LM framework [22].

To evaluate the robustness of our MoR algorithms, we trained the model using two distinct configurations, varying both the dataset and key hyperparameters. In the first configuration, the model was trained for one trillion tokens on a sample from the Nemotron-4 training data [23], with a cosine learning rate schedule annealing from 3×10^{-4} to 3×10^{-5} and a batch size of 1024. The second configuration used one trillion tokens from the higher-quality Nemotron-H dataset [24], a cosine learning rate schedule annealing from 1.2×10^{-3} to 3×10^{-6} , and a batch size of 1536. These details are summarized in Table 1. The second configuration consistently achieved lower training loss and superior scores on downstream tasks.

Table 1: A comparison of the two training configurations.

Parameter	Configuration 1	Configuration 2
Training Data	Nemotron4 [23]	NemotronH [24]
Training Tokens	1 Trillion	1 Trillion
LR Schedule	Cosine	Cosine
Peak Learning Rate	3×10^{-4}	1.2×10^{-3}
Final Learning Rate	3×10^{-5}	3×10^{-6}
Batch Size	1024	1536

To simulate the effects of quantization while maintaining a standard training pipeline, we employed a fake quantization framework, illustrated in Figure 4. In this process, a BF16 input block is first scaled and quantized to the target format (e.g., E4M3). It is then immediately dequantized back to BF16 and de-scaled to its original numerical range. The output tensor therefore remains in the BF16 format, but it carries the information loss characteristic of the lower-precision representation.

In the following sections, we present a comprehensive analysis of the tensor-level MoR algorithm, including its impact on model quality across multiple block dimensions and a detailed analysis of its decision-making process. Our evaluation of the sub-tensor MoR algorithm is more concise, focusing primarily on its effect on final model quality.

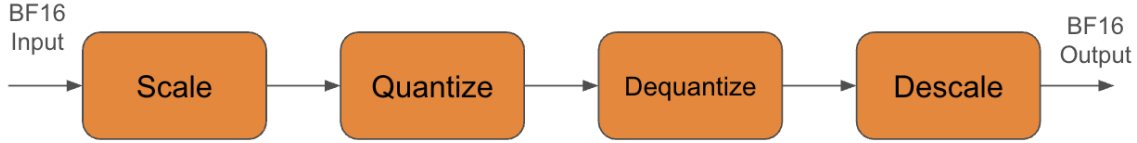


Figure 4: The fake quantization workflow. The input and output data type are kept in BF16 precision, but the process simulates the precision loss of the target format.

4.1 Experiments for MoR at Tensor Granularity

4.1.1 MoR with Different Partition Strategies

To study how MoR behaves across different scaling granularities, we implemented and evaluated three distinct partition strategies for the tensor-level MoR algorithm:

- **Per-Block:** Computes one scaling factor for each 128×128 block of the tensor.
- **Per-Tensor:** Computes a single scaling factor for the entire tensor.
- **Per-Channel:** Computes a scaling factor for each row of the first GEMM operand and each column of the second, aligned with the dot-product dimension.

To ensure a fair comparison, we used the same acceptance threshold, th_{E4M3} , for all three strategies.

To select an appropriate threshold, we analyzed the activation, weight, and gradient tensors from a reference BF16 training run, collected near the end of training. We calculated the relative error that would result from quantizing these tensors to E4M3. Based on this analysis, we determined that a threshold of $th_{E4M3} = 4.5\%$ would quantize approximately 95% of the tensors to E4M3, while leaving the remaining 5% in BF16. This ratio provided a reasonable starting point for our experiments, so we used a fixed threshold of 4.5% for all tensor-level MoR variants.

The training dynamics for both training configurations are shown in Figures 5 and 6. Across both configurations, the training loss, validation loss, and parameter norm curves for all MoR variants closely track the BF16 baseline, indicating stable training process.

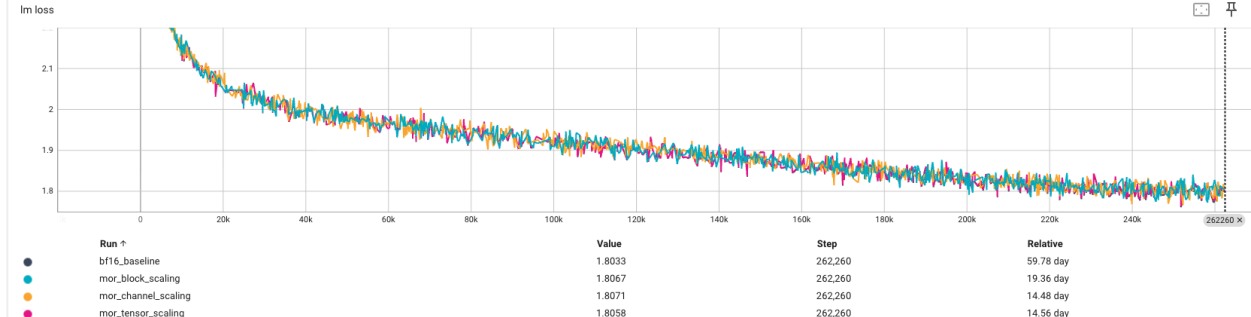
Table 2 summarizes the final loss values and downstream task evaluation scores using the last saved checkpoint. The final training and validation losses for all MoR variants are within 0.5% of the BF16 baseline. While the downstream task evaluations show higher variance, the three MoR strategies generally achieve on-par results with the baseline (most differences are about 1%). Some benchmarks, such as OpenBookQA and CommonSenseQA under Configuration 1, show a larger deviation. We attribute this to checkpoint selection sensitivity; selecting for the best score across several recent checkpoints, rather than just the last one, closes this gap significantly. For example, the best OpenBookQA scores under Configuration 1 are 42.2 (Block), 42.2 (Tensor), and 42.8 (Channel), which are competitive with the 42.8 baseline; similarly, the best CommonSenseQA under Configuration 1 are 37.84 (Block), 32.76 (Tensor), and 34.32 (Channel), which are closer to the 34.32 baseline.

This trend of strong performance is further supported by the MMLU 5-shot evaluation progress, shown in Figure 7. The MoR curves track the BF16 baseline closely, with the per-channel MoR variant slightly outperforming the baseline in Configuration 2. These observations lead us to conclude that the tensor-level MoR algorithm is robust across different partitioning strategies and training configurations, consistently achieving model quality on-par with the BF16 baseline.

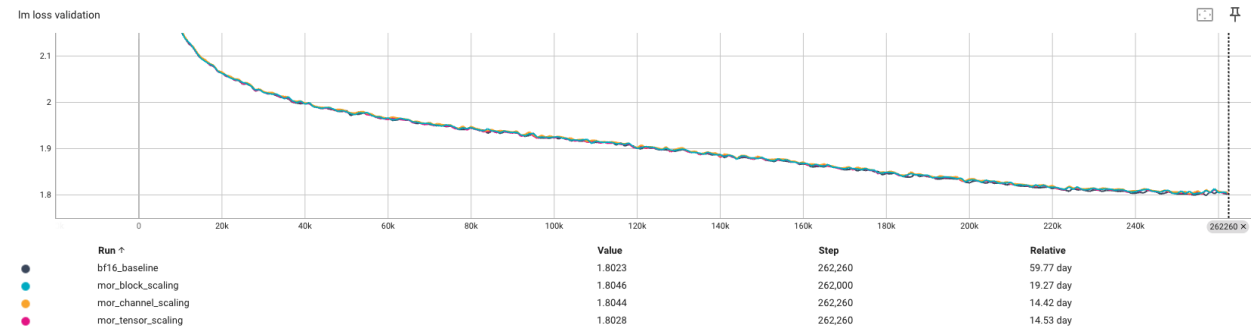
4.1.2 Ablation Study on MoR Settings

In this section, we study how different MoR settings affect model quality. We performed three sets of ablation experiments using the per-block partitioning strategy and the first training configuration.

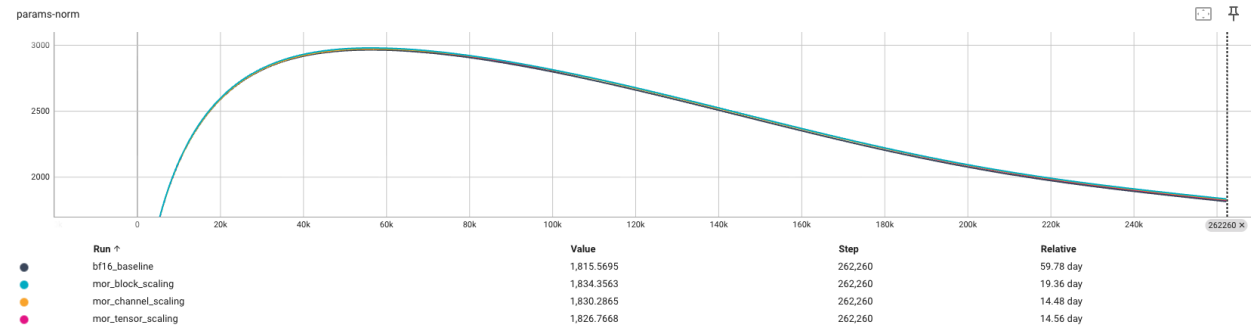
The first experiment varies the **block dimension**. By reducing the block size from 128×128 to 64×64 , we hypothesize that the more granular scaling factors will lead to a more accurate quantized representation. The second experiment adjusts the **acceptance threshold**. By increasing the threshold from 4.5% to 5.0%, we allow more tensors with higher relative error to be quantized to E4M3, potentially impacting model quality. The third experiment compares different **scaling algorithms**: our proposed GAM scaling, a simpler E8M0 per-block scaling, and the standard per-block FP32 amax scaling.



(a) Training Loss.



(b) Validation Loss.



(c) L2 Norm of the Parameters.

Figure 5: Training loss, validation loss, and the parameter L2 Norm using the first training configuration. In the legend, from top to bottom, the curves represent: BF16 Baseline, MoR Per-Block, MoR Per-Channel, and MoR Per-Tensor.

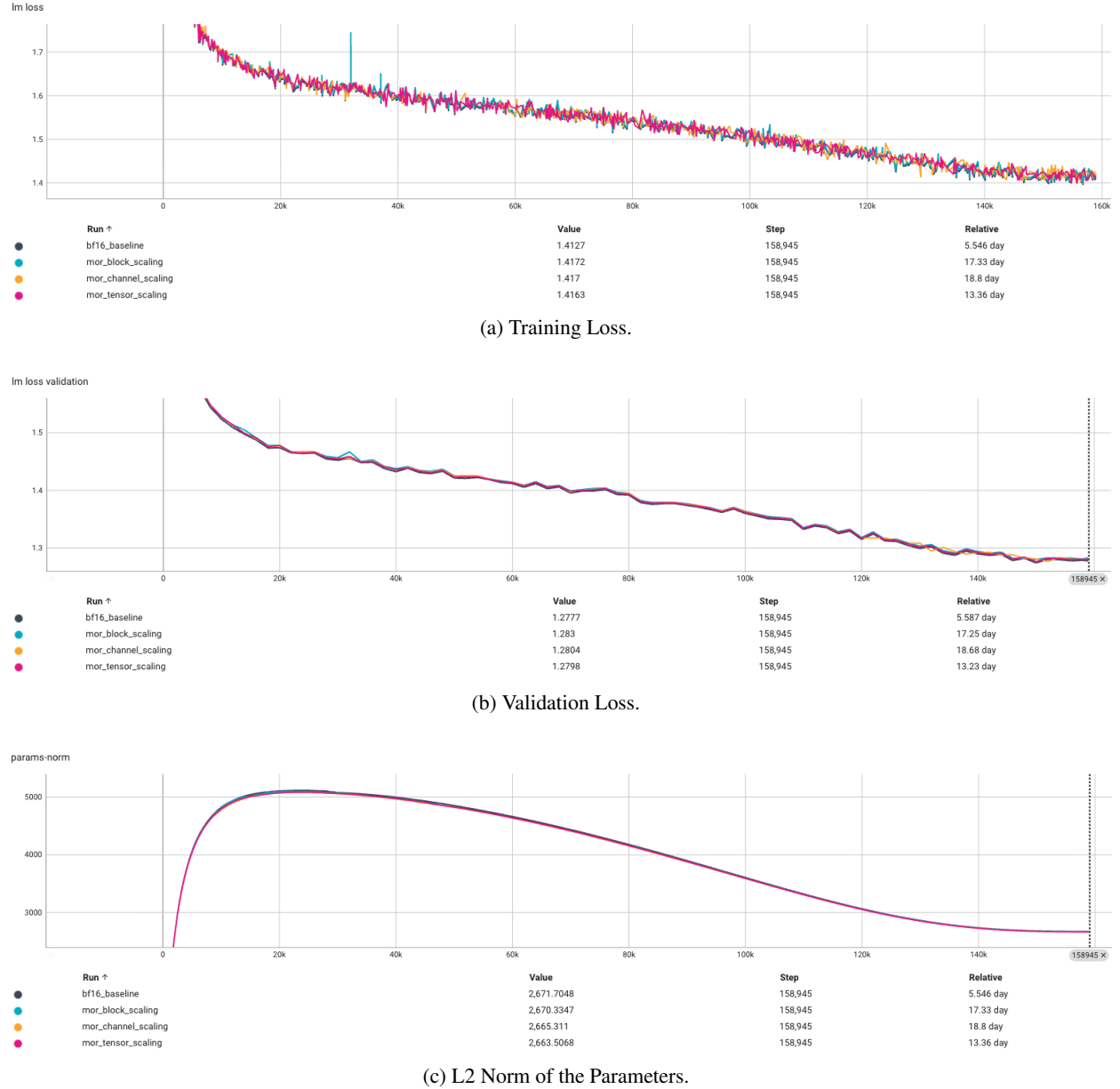
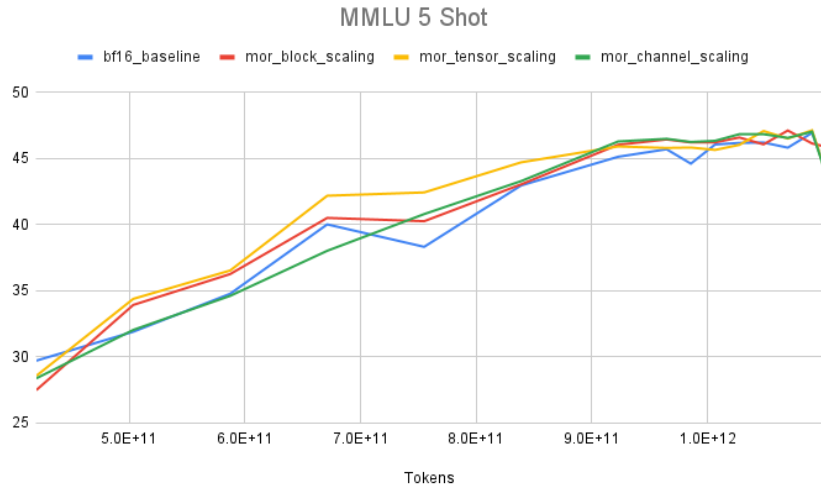
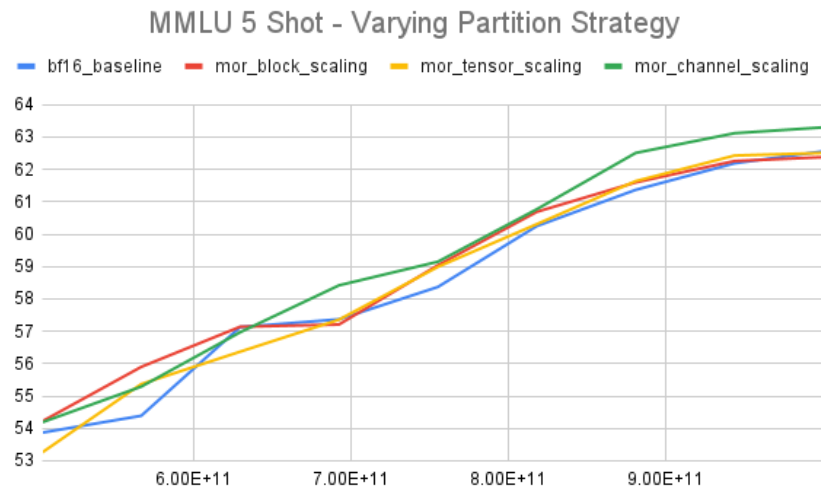


Figure 6: Training loss, validation loss, and the parameter L2 Norm using the second training configuration. In the legend, from top to bottom, the curves represent: BF16 Baseline, MoR Per-Block, MoR Per-Channel, and MoR Per-Tensor.



(a) Training Configuration 1.



(b) Training Configuration 2.

Figure 7: The MMLU 5-shot scores over the training progress for the two training configurations.

Table 2: Model quality comparison with varying partition strategies.

Metric	Configuration 1				Configuration 2			
	BF16	Block	Tensor	Channel	BF16	Block	Tensor	Channel
Training Loss	1.8033	1.8067	1.8058	1.8071	1.4127	1.4172	1.4163	1.4170
Validation Loss	1.8023	1.8046	1.8028	1.8044	1.2777	1.2830	1.2798	1.2804
MMLU	44.72	45.95	44.61	44.50	62.56	62.38	62.51	63.30
WinoGrande	66.69	66.77	66.69	67.40	69.85	72.38	71.67	70.64
PIQA	78.45	79.16	77.69	78.40	81.61	80.63	81.07	80.96
HellaSwag	74.93	74.84	74.85	75.02	77.56	77.47	77.82	77.67
Arc-Easy	73.48	73.36	73.91	74.24	83.67	83.88	82.41	81.82
Arc-Challenge	41.30	43.34	42.24	42.24	54.78	58.19	56.48	56.23
OpenBookQA	42.80	39.80	40.40	41.80	44.00	45.20	44.80	45.20
SIQA	44.63	45.65	46.42	45.04	46.83	45.45	46.72	46.57
CommonSenseQA	34.32	34.23	30.88	26.37	67.65	65.93	66.34	64.78

The training dynamics for these experiments are summarized in Figure 8. All variants track the BF16 baseline closely, indicating stable training. Notably, the E8M0 scaling variant consistently achieved a slightly lower training and validation loss than the BF16 baseline. The final metrics and downstream evaluation scores are presented in Table 3. While final loss values are all within 0.5% of the baseline, the downstream task results show more variance. The standard FP32 amax scaling strategy, for instance, results in an MMLU score of 1.63% lower than the baseline. Conversely, some high-variance benchmarks like CommonSenseQA show unexpectedly large gains for the 64×64 and 5.0% threshold settings, which may be attributable to evaluation noise.

The MMLU performance over the course of training, shown in Figure 9, provides clearer insights. As expected, the smaller 64×64 block size closely tracks the baseline and the default 128×128 MoR performance, confirming the benefit of finer granularity. Increasing the threshold to 5.0% (quantizing more tensors to E4M3) results in a slight degradation in MMLU score in the later stages of training. The comparison of scaling algorithms in Figure 9(b) is particularly revealing. The E8M0 scaling factor tracks the BF16 baseline most closely, while the standard FP32 amax scaling creates a noticeable gap. This suggests that having a consistent mantissa across the tensor, a feature of both our GAM algorithm and the E8M0 format (which has no mantissa bits), plays a crucial role in maintaining stable training dynamics and final model performance.

Table 3: Model quality comparison with varying MoR settings.

Metric	BF16	Block 128x128	Block 64x64	Th5.0%	Amax Factor	E8M0 Factor
Training Loss	1.8033	1.8067	1.8075	1.8065	1.8066	1.7956
Validation Loss	1.8023	1.8046	1.8084	1.8052	1.8037	1.7946
MMLU	44.72	45.95	46.37	44.37	43.99	45.62
WinoGrande	66.69	66.77	67.17	67.56	68.75	67.48
PIQA	78.45	79.16	77.86	78.18	77.48	79.11
HellaSwag	74.93	74.84	75.08	75.06	75.13	74.69
Arc-Easy	73.48	73.36	73.27	73.70	73.06	72.60
Arc-Challenge	41.30	43.34	42.32	42.24	42.06	42.75
OpenBookQA	42.80	39.80	41.80	41.40	39.40	40.40
SIQA	44.63	45.65	45.65	45.04	44.83	44.47
CommonSenseQA	34.32	34.23	39.15	39.39	33.74	36.61

4.1.3 Tensor Statistics

The MoR framework’s reliance on relative error allows us to collect detailed statistics for each tensor on a per-mini-batch basis. This section presents these statistics, captured over the course of training, to provide deeper insights into the algorithm’s dynamic decision-making process.

The overall percentage of tensors that fall back to BF16 throughout training is summarized in Figure 10. The second training configuration, which uses higher-quality data, consistently requires more tensors to remain in BF16. Across

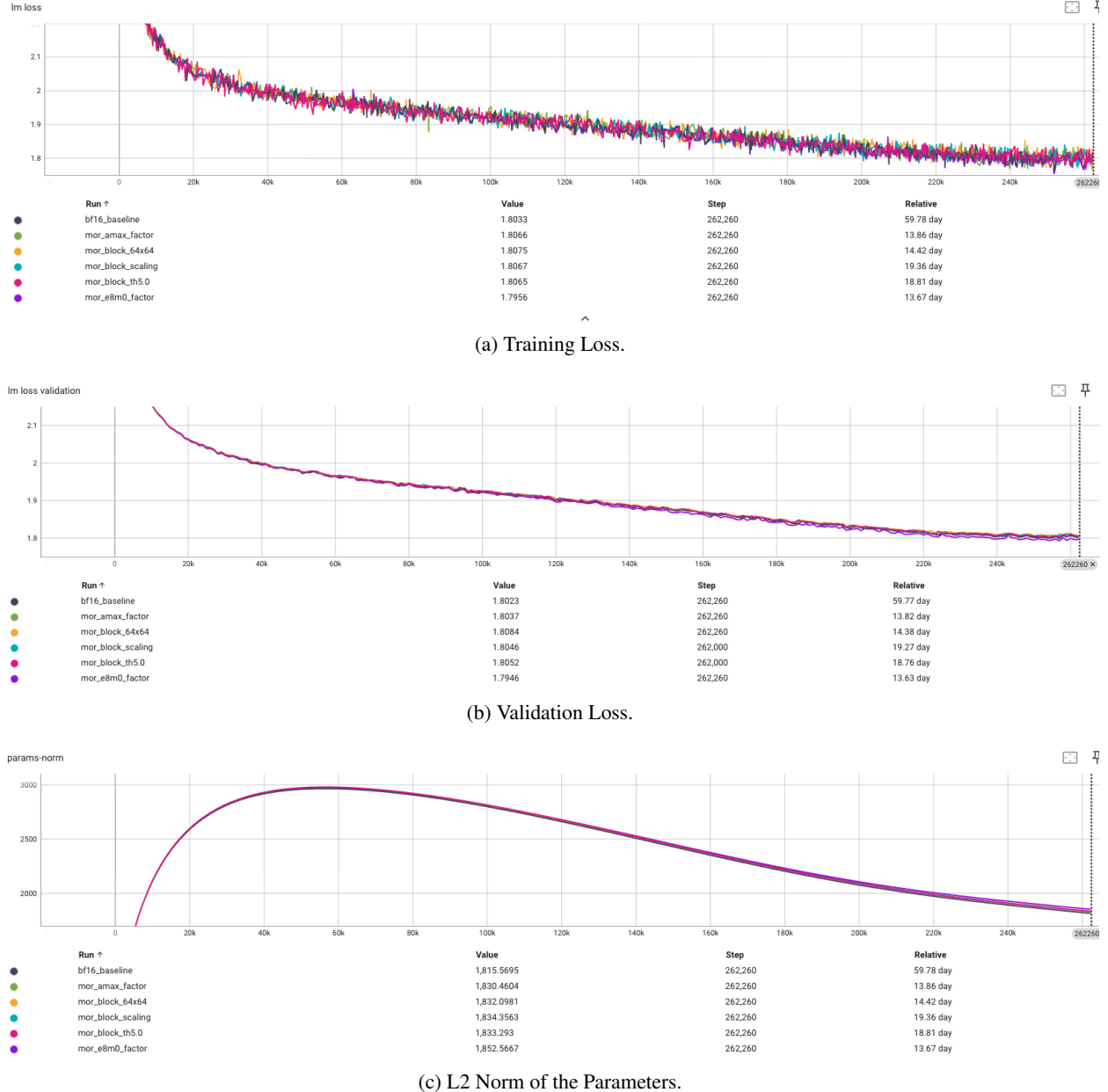


Figure 8: Training loss, validation loss, and the parameter L2 Norm using the first training configuration. In the legend, from top to bottom, the curves represent: BF16 Baseline, MoR FP32 Amax, MoR 64x64 Block, MoR 128x128 Block (Default), MoR 5.0% Threshold, and MoR E8M0.

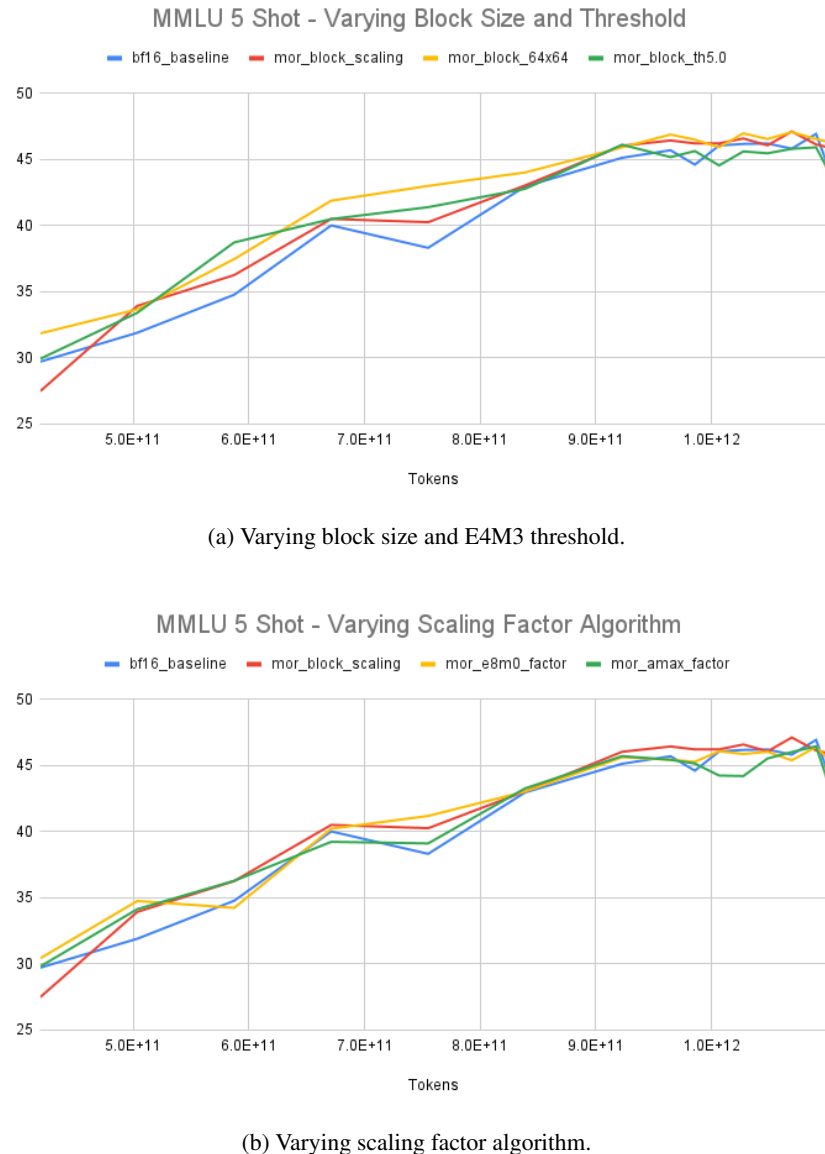


Figure 9: The MMLU 5-shot scores over the training progress when varying the MoR block size, the MoR E4M3 threshold, and the scaling factor algorithms.

the three partitioning strategies, per-channel scaling exhibits the highest quantization efficiency, with only 1.62% and 4.07% of tensors falling back to BF16 for the first and second configurations, respectively. Conversely, the per-tensor strategy is the least efficient, requiring the most fallbacks.

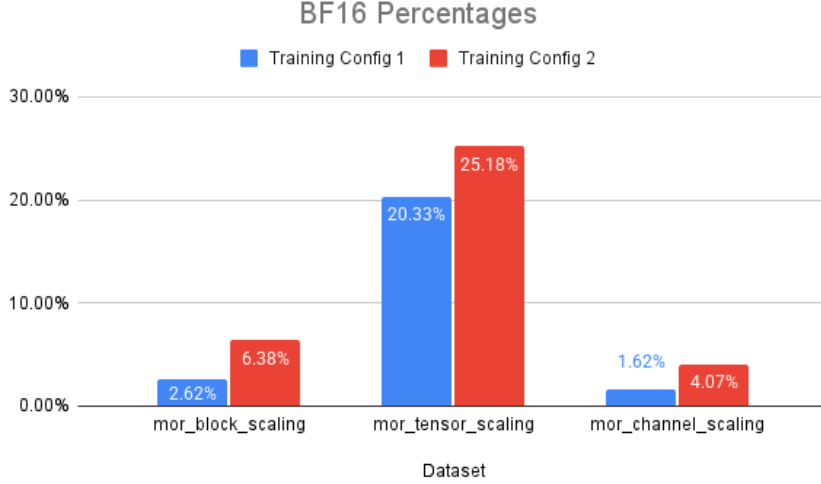


Figure 10: Percentage of tensors that fall back to the BF16 type.

To visualize the distribution of relative error, we generate periodic histograms for each tensor, as annotated in Figure 11. The **x-axis** of our heatmaps represents the bins of these histograms, where each bin covers a 0.5% range of relative error. The first bin corresponds to the normalized counts for relative error $< 0.5\%$, and second bin corresponds to the normalized counts for $0.5\% \leq \text{relative error} < 1.0\%$, and so forth. The right most bin corresponds to relative error $> 5.5\%$ and beyond. The blue vertical line marks the E4M3 threshold 4.5%. So tensors to the left of the line will be quantized to E4M3, and tensors to the right of the line will fall back to BF16. The **y-axis** in the heatmap is the name of the tensor. "decoder.layer.n" means this is the nth transformer block. "mlp" vs "self_attention" means this is the MLP module or the attention module. "linear_qkv", "linear_proj", "fc1", "fc2" are the linear modules in the attention/MLP modules. "grad", "weight", "input/ln_out" are the gradient, weight, and activation tensors accessed in the linear module.

We also collected finer-grained statistics to learn the distribution of the relative error. The statistics and the visualization can be illustrated in Figure 11. When we compute the relative error of one tensor, we will get one count, and we can accumulate the count to a histogram. The x axis in the heatmap visualization is the relative error histogram. Each bin covers the relative error value in a 0.5% range. The first bin corresponds to the normalized counts for relative error $< 0.5\%$, and second bin corresponds to the normalized counts for $0.5\% \leq \text{relative error} < 1.0\%$, and so forth. The right most bin corresponds to relative error $> 5.5\%$ and beyond. The blue vertical line marks the E4M3 threshold 4.5%. So tensors to the left of the line will be quantized to E4M3, and tensors to the right of the line will fall back to BF16. The y axis in the heatmap is the name of the tensor. "decoder.layer.n" means this is the nth transformer block. "mlp" vs "self_attention" means this is the MLP module or the attention module. "linear_qkv", "linear_proj", "fc1", "fc2" are the linear modules in the attention/MLP modules. "grad", "weight", "input/ln_out" are the gradient, weight, and activation tensors accessed in the linear module.

One mini-batch contributes to one count in the histogram. So the sum over each row is the number of mini-batches that are processed. We then normalize the counts over each row into a number between 0 and 1. The normalized counts are visualized with different heat colors, with darker color implying denser counts in the histogram bin, and lighter color implying sparser counts in the histogram bin. In order to see how the distribution changes over time, we reset the histogram every 6000 steps.

There are 32 transformer blocks in the model, each block has 4 linear layers, and each layer has 3 tensors. In total there are $32 \times 4 \times 3 = 384$ rows in the heatmap. The full heatmaps are too large to display. We therefore present representative subsets in the following analyses.

Analysis of Per-Block Scaling (Configuration 1) We begin by analyzing the per-block strategy. At the end of training, we can see the heatmap of the first three and last three transformer blocks during the forward pass in Figure 12. As illustrated in the heatmap, most of the tensors have relative error well below 2.5%. The only exception is the FC2

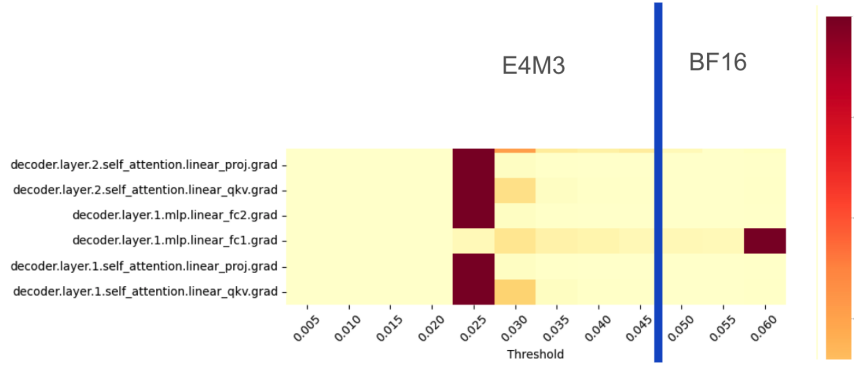


Figure 11: Annotation for the relative error histogram visualization. The x axis is the relative error histogram bins. The y axis is the name of the tensor.

activation tensor. For the first layer, the majority of the counts are in the last bin, which is relative error $> 5.5\%$. So MoR primarily uses BF16 to represent this tensor. Fortunately, the histogram density shifts left when the transformer block number increases. At the 3rd transformer block, the majority of the mass has already been below the 4.5% threshold, and are then quantized to E4M3. For the last three layers, the FC2 activation tensor is still the tensor with higher relative error. But the error is within the 4.5% bound. So these tensors are still quantized to E4M3. The heatmap for the backward pass is shown in Figure 13. For the last layer, all the gradient tensors have quite high relative errors. After the last layer, the gradient tensors for the linear_qkv module and the fc1 module has higher relative error. But the relative error is shifting towards left when the transformer block number decreases. So most of the gradient tensors are still quantized to E4M3. But there is an interesting outlier at the 1st layer. The gradient tensor for the FC1 module has quite high relative error.

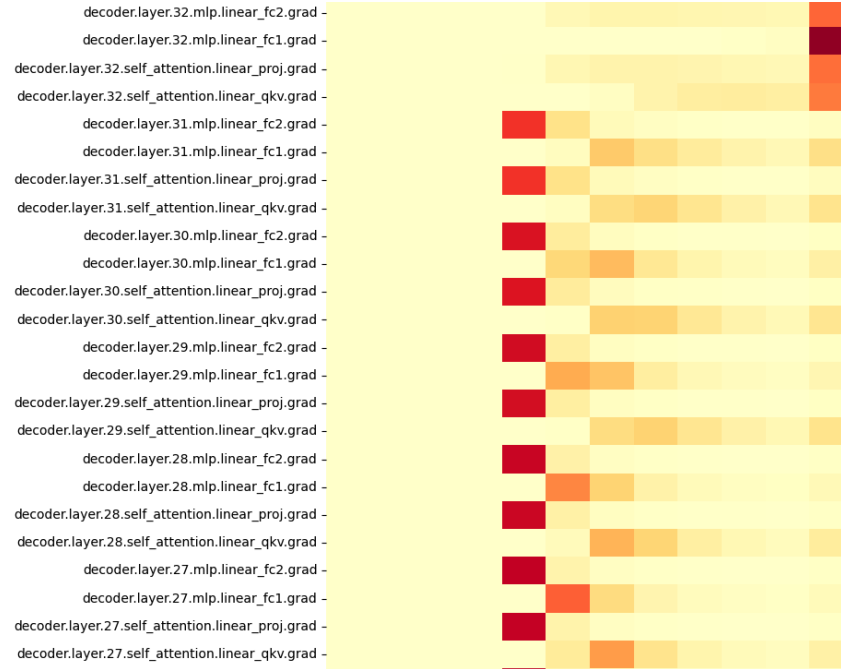
As the first layer is very special, we visualize the relative error based on training steps and visualize in Figure 14. In this heatmap, the y-axis now becomes the training step. So from the top to bottom reveals how the relative error distribution changes when we train with more data. A key observation is that the FC2 activation tensor and the FC1 gradient tensor do not start with high relative error. They start with smaller relative error, but when training with more steps, the relative error grows and eventually exceeds the 4.5% threshold. This means that at the beginning phase of training, the tensors are having smaller dynamic ranges, and can be represented by E4M3 properly. But when training make more progress, the dynamic range in the block increases over time, and eventually we will need to fall back to BF16 to control the quantization error. This ability to adapt to changing tensor statistics over time is a core strength of the MoR framework.

Comparing Training Configurations The next step we will study the differences between the first training configuration and the second training configuration using the block scaling partition strategy. The heatmap for the first and last three transformer blocks are summarized in Figure 15. Compared to Figure 12, there are definitely more tensors with much higher relative errors. In the heatmap, all the FC1 weight, the FC2 activation, and FC2 weight tensors have much higher relative error in this training config. Again, there is a trend to shift towards left with increasing the transformer block number, and there are no more BF16 fall backs after the 9th transformer block. The heatmaps for the backward pass is shown in Figure 16. Again, the linear_qkv and the FC1 gradient tensors are the ones with higher relative errors. But this time the FC1 gradient tensor has higher relative error for all the first 6 layers instead of just the 1st layer as in the first training config. This explains why we see the BF16 percentage has increased from 2.62% to 6.38% when we change the training config from the first config to the second config. The results demonstrate that training dynamics are highly dependent on the dataset and hyperparameters, and that MoR successfully adapts its quantization decisions to these different conditions.

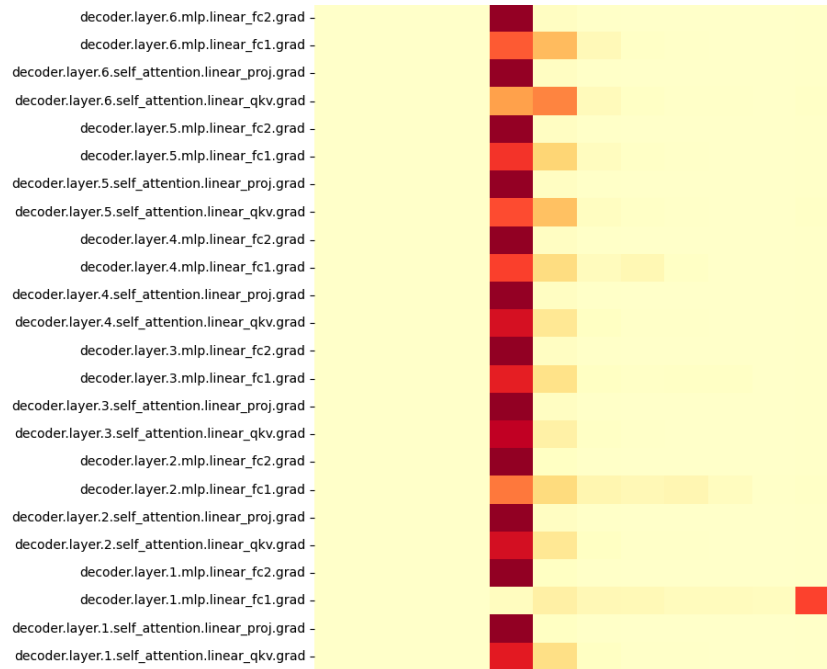
Comparing Partitioning Strategies The heatmaps also explain the quantization decision making differences between partitioning strategies. The **per-tensor** strategy has the highest BF16 fallback rate because its single scaling factor must cover the dynamic range of the entire tensor. As long as there are 2.4% values that are flushed to zero, then the relative error for the tensor will exceed 4.5% and will fall back to BF16. So it makes sense for the per-tensor partition strategy to have much higher BF16 fall back ratios. The heatmap can show exactly which tensors are now falling back to BF16. As shown in Figure 17, the additional tensors that fall back to BF16 are the tensors in the middle layers. In the forward pass, all the FC2 activations from all layers fall back to BF16. Similarly, the gradient tensors for the linear_qkv and fc1 modules also have increased falling back rate in all layers. This is why the amount of BF16 tensors is much larger for the tensor scaling partition strategy compared to the block scaling strategy.



Figure 12: Heatmap for the MoR block scaling algorithm in the forward pass.



(a) Last six transformer blocks.



(b) First six transformer blocks.

Figure 13: Heatmap for the MoR block scaling algorithm in the backward pass.

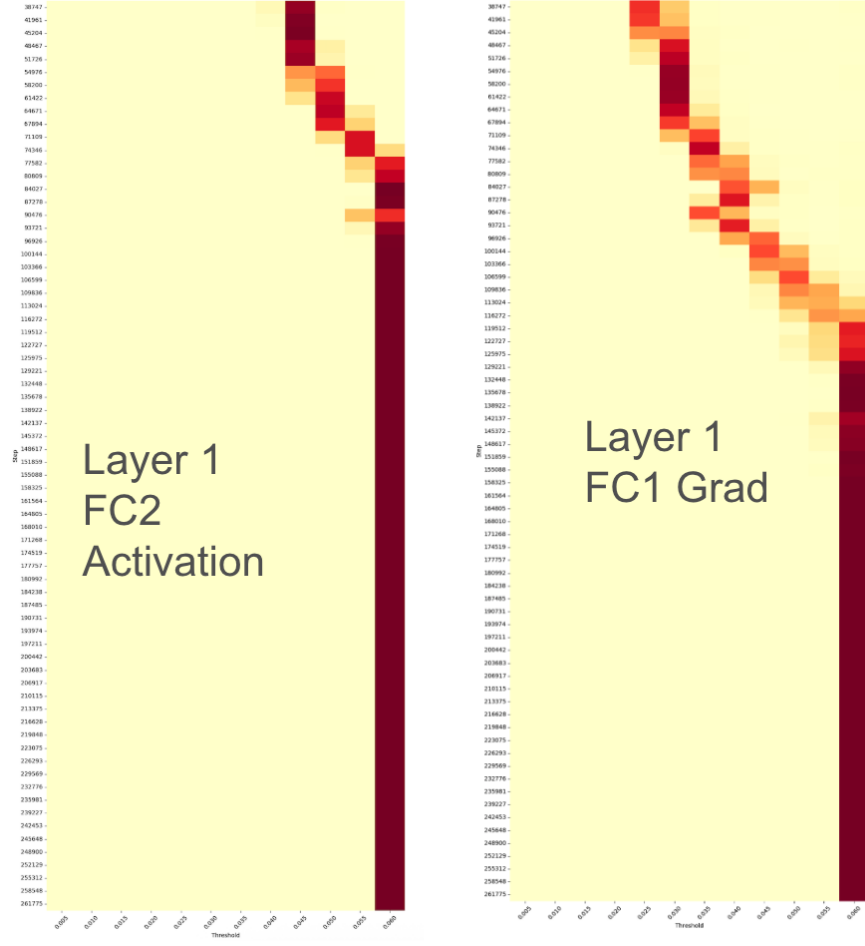


Figure 14: Heatmaps for the first transformer block. The x axis is the relative error histogram bins. The y axis is the training step.

Conversely, the per-channel strategy is the most efficient. The forward heatmap for the first two transformer blocks is in Figure 18, and the backward heatmaps for the first and last four transformer blocks are in Figure 19. As illustrated in the heatmap, each tensor needs to be partitioned and quantized based on rows and columns according to the dot product dimension, and the relative error can differ dramatically depending on the partitioning direction. In the forward pass, the only tensor that needs BF16 for the per-block strategy is the FC2 activation tensor. When using the per-channel partition strategy, the row partition has high relative errors, but the column partition has much smaller relative errors. So we only need BF16 for the row partition, but not the column partition. Similarly, for all the gradient tensors in the backward pass, one direction has much smaller relative error. This fine-grained selection reduces the total amount of tensors kept in BF16 by nearly half compared to the per-block strategy.

These detailed visualizations confirm that the MoR algorithm successfully adapts its quantization decisions based on tensor numerics at runtime, making it robust across different partitioning strategies and training configurations.

4.2 Experiments for MoR at Sub-Tensor Granularity

In this section, we evaluate the model quality of the sub-tensor MoR algorithms detailed in Section 3.2. We compare two recipes for partitioning at the 128×128 block level: the "Three-Way Selection" algorithm, which chooses between E4M3, E5M2, and BF16, and the "Two-Way Selection" algorithm, which chooses only between E4M3 and BF16. Both were evaluated using the first training configuration 1.

The training dynamics are presented in Figure 20. While the Two-Way Selection algorithm's loss curves closely track the BF16 baseline, the Three-Way Selection variant surprisingly achieves a slightly better final training and validation loss.



(a) First three transformer blocks.

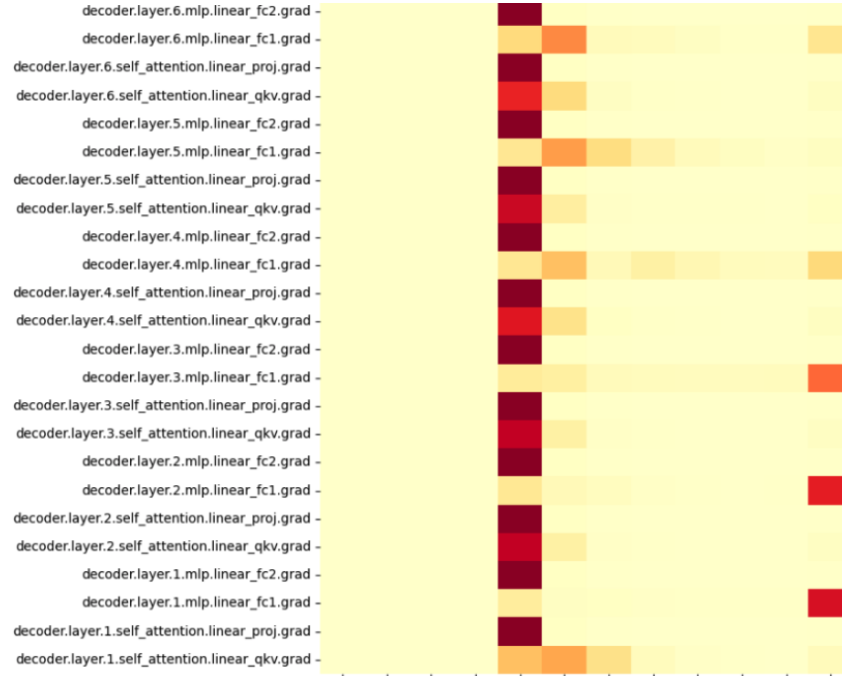


(b) Last three transformer blocks.

Figure 15: Heatmap for the MoR block scaling algorithm in the forward pass, using the second training configuration.



(a) Last six transformer blocks.

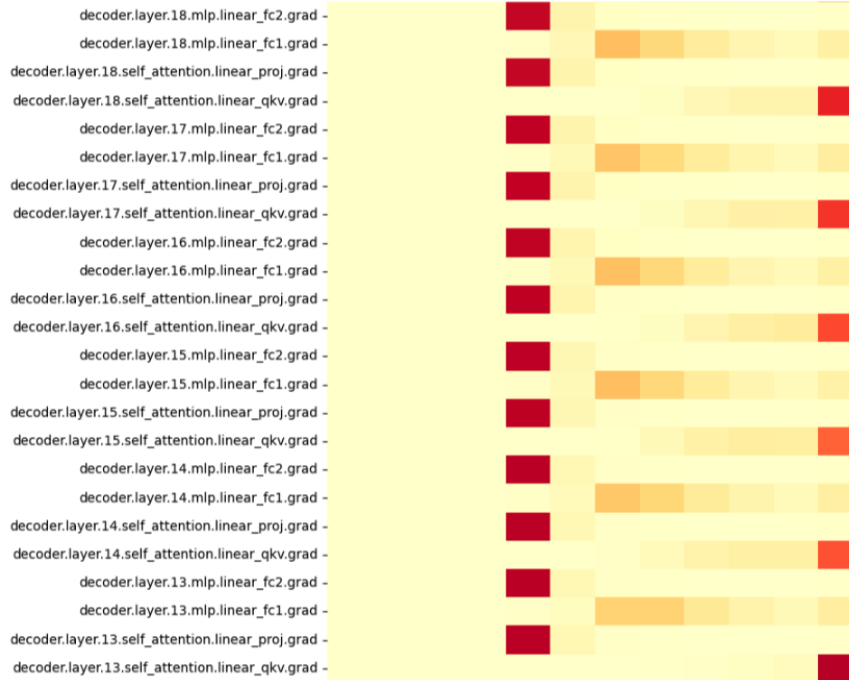


(b) First six transformer blocks.

Figure 16: Heatmap for the MoR block scaling algorithm in the backward pass, using the second training configuration.



(a) Middle three transformer blocks in the forward pass.



(b) Middle six transformer blocks in the backward pass.

Figure 17: Heatmap for the MoR tensor scaling algorithm, using the first training configuration.



Figure 18: First two transformer blocks in the forward pass.

However, this apparent advantage does not translate to downstream task evaluation scores, as shown in Table 4 and Figure 21. The Two-Way Selection algorithm achieves results that are on-par with, and on some tasks superior to, the BF16 baseline. In contrast, the Three-Way Selection algorithm exhibits a significant quality degradation on most downstream benchmarks, which is particularly evident in the MMLU performance curve.

The divergence between the validation loss and downstream task evaluation scores suggests that the Three-Way Selection algorithm overfits to the training and validation data distributions. While the additional flexibility of the E5M2 format helps minimize loss on in-distribution data, it appears to harm the model’s ability to generalize to the different data distributions of the evaluation benchmarks. Investigating the precise mechanism by which the inclusion of E5M2 leads to this overfitting behavior will be continued in future works.



(a) Last four transformer blocks.



(b) First four transformer blocks.

Figure 19: Heatmap for the MoR channel scaling algorithm in the backward pass, using the first training configuration.

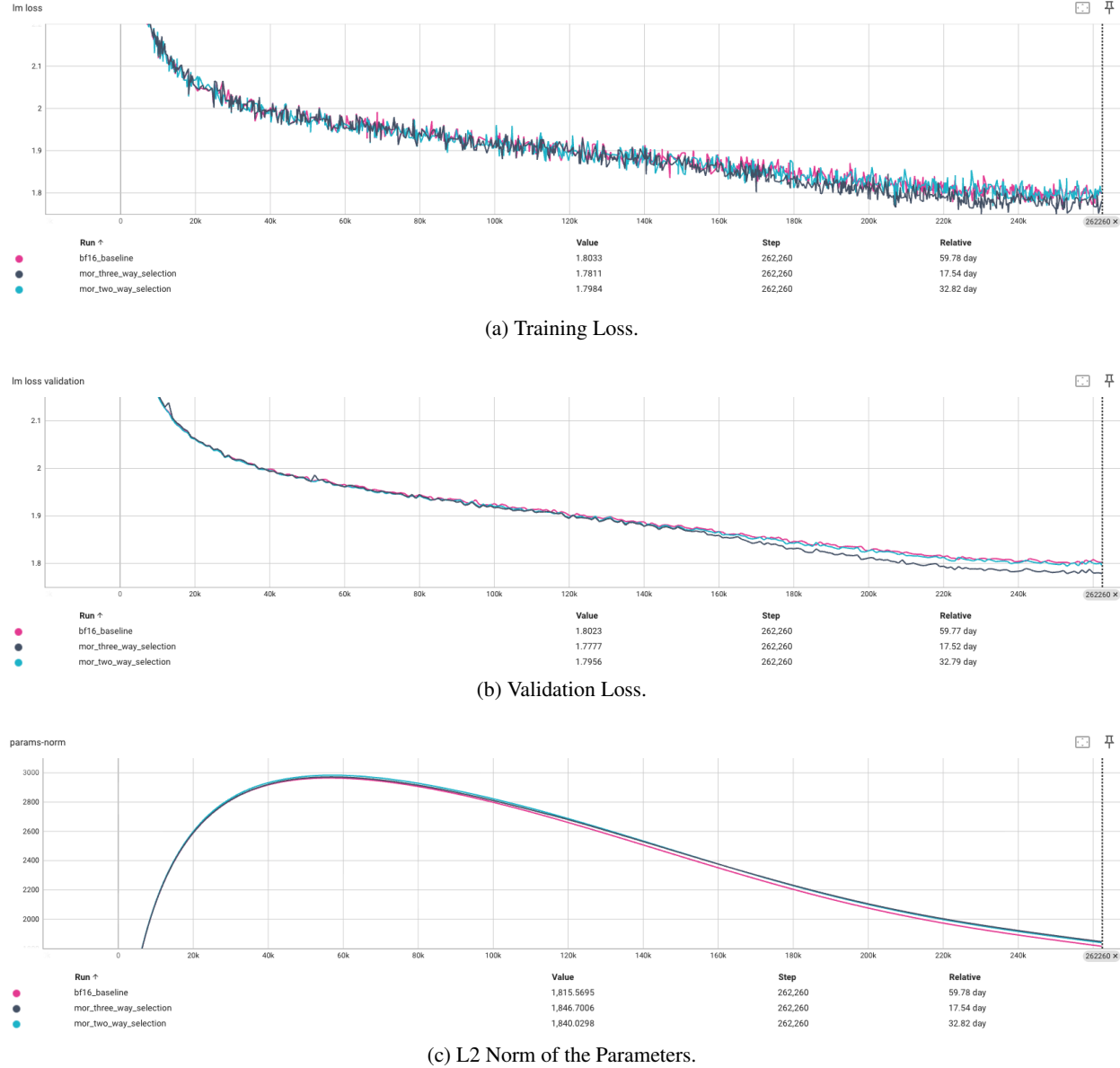


Figure 20: Training loss, validation loss, and the parameter L2 Norm using the first training configuration.

Table 4: Model quality comparison for different MoR subtensor algorithms.

Metric	BF16	Two-Way Selection	Three-Way Selection
Training Loss	1.8033	1.7984	1.7811
Validation Loss	1.8023	1.7956	1.7777
MMLU	44.72	46.56	42.84
WinoGrande	66.69	68.35	66.61
PIQA	78.45	78.51	78.24
HellaSwag	74.93	74.67	73.58
Arc-Easy	73.48	74.24	71.13
Arc-Challenge	41.30	41.30	41.89
OpenBookQA	42.80	40.20	41.60
SIQA	44.63	45.70	44.01
CommonSenseQA	34.32	40.87	29.07

5 Conclusions

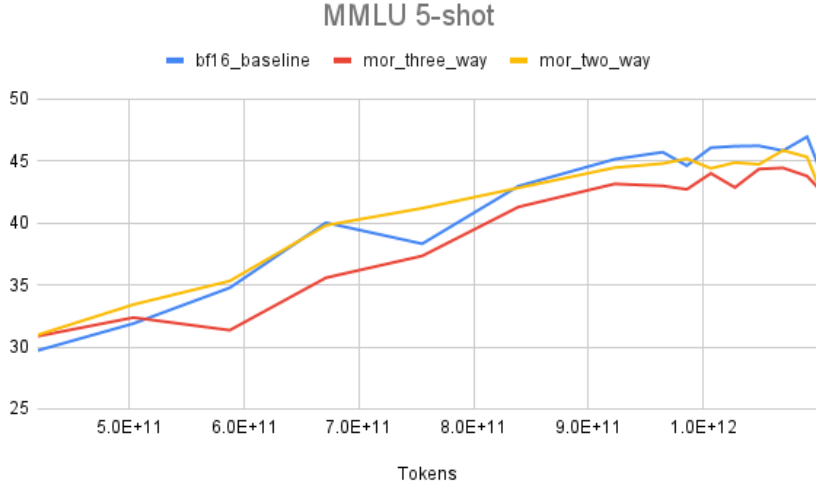


Figure 21: MMLU 5-shot scores for MoR subtensor algorithms.

In this paper, we introduced two primary contributions to the field of mixed-precision training. First, we proposed the Group Amax Mantissa (GAM) scaling algorithm, a novel method that accurately preserves the absolute maximum value of a tensor group, enhancing the precision of the scaling process. Second, we developed the Mixture-of-Representations (MoR) framework, a dynamic, metric-driven approach to selecting quantization formats at runtime.

Our experiments demonstrate that the tensor-level MoR algorithm is remarkably robust and effective. Using a single, empirically-derived relative error threshold of 4.5%, our method achieved on-par model quality with a standard BF16 baseline across three different partitioning strategies and two distinct training configurations. The approach is also highly efficient; our best-performing per-channel strategy successfully quantized over 98.38%/95.93% of tensors to E4M3 in the two training configurations, requiring only a small fraction to remain in high precision.

Furthermore, we presented preliminary but promising results for sub-tensor MoR. The two-way (E4M3/BF16) selection recipe also maintained model quality comparable to the baseline. While our investigation of this finer granularity is ongoing, we believe the flexibility of the sub-tensor approach holds significant potential for future work aimed at further optimizing the memory and compute footprints of large model training.

Acknowledgments

The authors wish to thank Dusan Stosic, Oleg Rybakov, Mohammad Shoeybi, Bryan Catanzaro, Rama Govindaraju, Mike Houston, Misha Smelyanskiy, Carlo del Mundo, Eric Chung, and Jonah Alben for their support and valuable feedback throughout this research.

References

- [1] Jared Kaplan, Sam McCandlish, Tom Henighan, Tom B. Brown, Benjamin Chess, Rewon Child, Scott Gray, Alec Radford, Jeffrey Wu, and Dario Amodei. Scaling laws for neural language models, 2020.
- [2] Aaron Grattafiori, Abhimanyu Dubey, Abhinav Jauhri, Abhinav Pandey, Abhishek Kadian, Ahmad Al-Dahle, Aiesha Letman, Akhil Mathur, Alan Schelten, Alex Vaughan, Amy Yang, Angela Fan, Anirudh Goyal, Anthony Hartshorn, Aobo Yang, Archi Mitra, Archie Sravankumar, Artem Korenev, Arthur Hinsvark, Arun Rao, Aston Zhang, Aurelien Rodriguez, Austen Gregerson, Ava Spataru, Baptiste Roziere, Bethany Biron, Binh Tang, Bobbie Chern, Charlotte Caucheteux, Chaya Nayak, Chloe Bi, Chris Marra, Chris McConnell, Christian Keller, Christophe Touret, Chunyang Wu, Corinne Wong, Cristian Canton Ferrer, Cyrus Nikolaidis, Damien Allonsius, Daniel Song, Danielle Pintz, Danny Livshits, Danny Wyatt, David Esiobu, Dhruv Choudhary, Dhruv Mahajan, Diego Garcia-Olano, Diego Perino, Dieuwke Hupkes, Egor Lakomkin, Ehab AlBadawy, Elina Lobanova, Emily Dinan, Eric Michael Smith, Filip Radenovic, Francisco Guzmán, Frank Zhang, Gabriel Synnaeve, Gabrielle

Lee, Georgia Lewis Anderson, Govind Thattai, Graeme Nail, Gregoire Mialon, Guan Pang, Guillem Cucurell, Hailey Nguyen, Hannah Korevaar, Hu Xu, Hugo Touvron, Iliyan Zarov, Imanol Arrieta Ibarra, Isabel Kloumann, Ishan Misra, Ivan Evtimov, Jack Zhang, Jade Copet, Jaewon Lee, Jan Geffert, Jana Vranes, Jason Park, Jay Mahadeokar, Jeet Shah, Jelmer van der Linde, Jennifer Billock, Jenny Hong, Jenya Lee, Jeremy Fu, Jianfeng Chi, Jianyu Huang, Jiawen Liu, Jie Wang, Jiecao Yu, Joanna Bitton, Joe Spisak, Jongsoo Park, Joseph Rocca, Joshua Johnstun, Joshua Saxe, Junteng Jia, Kalyan Vasudevan Alwala, Karthik Prasad, Kartikeya Upasani, Kate Plawiak, Ke Li, Kenneth Heafield, Kevin Stone, Khalid El-Arini, Krithika Iyer, Kshitiz Malik, Kuenley Chiu, Kunal Bhalla, Kushal Lakhotia, Lauren Rantala-Yeary, Laurens van der Maaten, Lawrence Chen, Liang Tan, Liz Jenkins, Louis Martin, Lovish Madaan, Lubo Malo, Lukas Blecher, Lukas Landzaat, Luke de Oliveira, Madeline Muzzi, Mahesh Pasupuleti, Mannat Singh, Manohar Paluri, Marcin Kardas, Maria Tsimpoukelli, Mathew Oldham, Mathieu Rita, Maya Pavlova, Melanie Kambadur, Mike Lewis, Min Si, Mitesh Kumar Singh, Mona Hassan, Naman Goyal, Narjes Torabi, Nikolay Bashlykov, Nikolay Bogoychev, Niladri Chatterji, Ning Zhang, Olivier Duchenne, Onur Çelebi, Patrick Alrassy, Pengchuan Zhang, Pengwei Li, Petar Vasic, Peter Weng, Prajjwal Bhargava, Pratik Dubal, Praveen Krishnan, Punit Singh Koura, Puxin Xu, Qing He, Qingxiao Dong, Ragavan Srinivasan, Raj Ganapathy, Ramon Calderer, Ricardo Silveira Cabral, Robert Stojnic, Roberta Raileanu, Rohan Maheswari, Rohit Girdhar, Rohit Patel, Romain Sauvestre, Ronnie Polidor, Roshan Sumbaly, Ross Taylor, Ruan Silva, Rui Hou, Rui Wang, Saghar Hosseini, Sahana Chennabasappa, Sanjay Singh, Sean Bell, Seohyun Sonia Kim, Sergey Edunov, Shaoliang Nie, Sharan Narang, Sharath Raparthy, Sheng Shen, Shengye Wan, Shruti Bhosale, Shun Zhang, Simon Vandenhende, Soumya Batra, Spencer Whitman, Sten Sootla, Stephane Collot, Suchin Gururangan, Sydney Borodinsky, Tamar Herman, Tara Fowler, Tarek Sheasha, Thomas Georgiou, Thomas Scialom, Tobias Speckbacher, Todor Mihaylov, Tong Xiao, Ujjwal Karn, Vedanuj Goswami, Vibhor Gupta, Vignesh Ramanathan, Viktor Kerkez, Vincent Gonget, Virginie Do, Vish Vogeti, Vitor Albiero, Vladan Petrovic, Weiwei Chu, Wenhan Xiong, Wenyin Fu, Whitney Meers, Xavier Martinet, Xiaodong Wang, Xiaofang Wang, Xiaoqing Ellen Tan, Xide Xia, Xinfeng Xie, Xuchao Jia, Xuewei Wang, Yaelle Goldschlag, Yashesh Gaur, Yasmine Babaei, Yi Wen, Yiwen Song, Yuchen Zhang, Yue Li, Yuning Mao, Zacharie Delpierre Coudert, Zheng Yan, Zhengxing Chen, Zoe Papakipos, Aaditya Singh, Aayushi Srivastava, Abha Jain, Adam Kelsey, Adam Shajnfeld, Adithya Gangidi, Adolfo Victoria, Ahuva Goldstand, Ajay Menon, Ajay Sharma, Alex Boesenber, Alexei Baevski, Allie Feinstein, Amanda Kallet, Amit Sangani, Amos Teo, Anam Yunus, Andrei Lupu, Andres Alvarado, Andrew Caples, Andrew Gu, Andrew Ho, Andrew Poulton, Andrew Ryan, Ankit Ramchandani, Annie Dong, Annie Franco, Anuj Goyal, Aparajita Saraf, Arkabandhu Chowdhury, Ashley Gabriel, Ashwin Bharambe, Assaf Eisenman, Azadeh Yazdan, Beau James, Ben Maurer, Benjamin Leonhardi, Bernie Huang, Beth Loyd, Beto De Paola, Bhargavi Paranjape, Bing Liu, Bo Wu, Boyu Ni, Braden Hancock, Bram Wasti, Brandon Spence, Brani Stojkovic, Brian Gamido, Britt Montalvo, Carl Parker, Carly Burton, Catalina Mejia, Ce Liu, Changhan Wang, Changkyu Kim, Chao Zhou, Chester Hu, Ching-Hsiang Chu, Chris Cai, Chris Tindal, Christoph Feichtenhofer, Cynthia Gao, Damon Civin, Dana Beaty, Daniel Kreymer, Daniel Li, David Adkins, David Xu, Davide Testuggine, Delia David, Devi Parikh, Diana Liskovich, Didem Foss, Dingkang Wang, Duc Le, Dustin Holland, Edward Dowling, Eissa Jamil, Elaine Montgomery, Eleonora Presani, Emily Hahn, Emily Wood, Eric-Tuan Le, Erik Brinkman, Esteban Arcuate, Evan Dunbar, Evan Smothers, Fei Sun, Felix Kreuk, Feng Tian, Filippos Kokkinos, Firat Ozgenel, Francesco Caggioni, Frank Kanayet, Frank Seide, Gabriela Medina Florez, Gabriella Schwarz, Gada Badeer, Georgia Swee, Gil Halpern, Grant Herman, Grigory Sizov, Guangyi, Zhang, Guna Lakshminarayanan, Hakan Inan, Hamid Shojanazeri, Han Zou, Hannah Wang, Hanwen Zha, Haroun Habeeb, Harrison Rudolph, Helen Suk, Henry Aspegen, Hunter Goldman, Hongyuan Zhan, Ibrahim Damlaj, Igor Molybog, Igor Tufanov, Ilias Leontiadis, Irina-Elena Veličić, Itai Gat, Jake Weissman, James Geboski, James Kohli, Janice Lam, Japhet Asher, Jean-Baptiste Gaya, Jeff Marcus, Jeff Tang, Jennifer Chan, Jenny Zhen, Jeremy Reizenstein, Jeremy Teboul, Jessica Zhong, Jian Jin, Jingyi Yang, Joe Cummings, Jon Carvill, Jon Shepard, Jonathan McPhie, Jonathan Torres, Josh Ginsburg, Junjie Wang, Kai Wu, Kam Hou U, Karan Saxena, Kartikay Khandelwal, Katayoun Zand, Kathy Matosich, Kaushik Veeraraghavan, Kelly Michelena, Keqian Li, Kiran Jagadeesh, Kun Huang, Kunal Chawla, Kyle Huang, Lailin Chen, Lakshya Garg, Lavender A. Leandro Silva, Lee Bell, Lei Zhang, Liangpeng Guo, Licheng Yu, Liron Moshkovich, Luca Wehrstedt, Madian Khabsa, Manav Avalani, Manish Bhatt, Martynas Mankus, Matan Hasson, Matthew Lennie, Matthias Reso, Maxim Groshev, Maxim Naumov, Maya Lathi, Meghan Keneally, Miao Liu, Michael L. Seltzer, Michal Valko, Michelle Restrepo, Mihir Patel, Mik Vyatskov, Mikayel Samvelyan, Mike Clark, Mike Mace, Mike Wang, Miquel Jubert Hermoso, Mo Metanat, Mohammad Rastegari, Munish Bansal, Nandhini Santhanam, Natascha Parks, Natasha White, Navyata Bawa, Nayan Singh, Nick Egebo, Nicolas Usunier, Nikhil Mehta, Nikolay Pavlovich Laptev, Ning Dong, Norman Cheng, Oleg Chernoguz, Olivia Hart, Omkar Salpekar, Ozlem Kalinli, Parkin Kent, Parth Parekh, Paul Saab, Pavan Balaji, Pedro Rittner, Philip Bontrager, Pierre Roux, Piotr Dollar, Polina Zvyagina, Prashant Ratanchandani, Pritish Yuvraj, Qian Liang, Rachad Alao, Rachel Rodriguez, Rafi Ayub, Raghotham Murthy, Raghu Nayani, Rahul Mitra, RangaPrabhu Parthasarathy, Raymond Li, Rebekkah Hogan, Robin Battey, Rocky Wang, Russ Howes, Ruty Rinott, Sachin Mehta, Sachin Siby, Sai Jayesh Bondu, Samyak Datta, Sara Chugh, Sara Hunt, Sargun Dhillon, Sasha Sidorov,

Satadru Pan, Saurabh Mahajan, Saurabh Verma, Seiji Yamamoto, Sharadh Ramaswamy, Shaun Lindsay, Shaun Lindsay, Sheng Feng, Shenghao Lin, Shengxin Cindy Zha, Shishir Patil, Shiva Shankar, Shuqiang Zhang, Shuqiang Zhang, Sinong Wang, Sneha Agarwal, Soji Sajuyigbe, Soumith Chintala, Stephanie Max, Stephen Chen, Steve Kehoe, Steve Satterfield, Sudarshan Govindaprasad, Sumit Gupta, Summer Deng, Sungmin Cho, Sunny Virk, Suraj Subramanian, Sy Choudhury, Sydney Goldman, Tal Remez, Tamar Glaser, Tamara Best, Thilo Koehler, Thomas Robinson, Tianhe Li, Tianjun Zhang, Tim Matthews, Timothy Chou, Tzook Shaked, Varun Vontimitta, Victoria Ajayi, Victoria Montanez, Vijai Mohan, Vinay Satish Kumar, Vishal Mangla, Vlad Ionescu, Vlad Poenaru, Vlad Tiberiu Mihaiescu, Vladimir Ivanov, Wei Li, Wencheng Wang, Wenwen Jiang, Wes Bouaziz, Will Constable, Xiaocheng Tang, Xiaojian Wu, Xiaolan Wang, Xilun Wu, Xinbo Gao, Yaniv Kleinman, Yanjun Chen, Ye Hu, Ye Jia, Ye Qi, Yenda Li, Yilin Zhang, Ying Zhang, Yossi Adi, Youngjin Nam, Yu, Wang, Yu Zhao, Yuchen Hao, Yundi Qian, Yunlu Li, Yuzi He, Zach Rait, Zachary DeVito, Zef Rosnbrick, Zhaoduo Wen, Zhenyu Yang, Zhiwei Zhao, and Zhiyu Ma. The llama 3 herd of models, 2024. URL <https://arxiv.org/abs/2407.21783>.

[3] Shaden Smith, Mostafa Patwary, Brandon Norick, Patrick LeGresley, Samyam Rajbhandari, Jared Casper, Zhun Liu, Shrimai Prabhumoye, George Zerveas, Vijay Korthikanti, Elton Zhang, Rewon Child, Reza Yazdani Aminabadi, Julie Bernauer, Xia Song, Mohammad Shoeybi, Yuxiong He, Michael Houston, Saurabh Tiwary, and Bryan Catanzaro. Using deepspeed and megatron to train megatron-turing nlg 530b, a large-scale generative language model, 2022.

[4] OpenAI. GPT-4 Technical Report, 2023.

[5] DeepSeek-AI, Aixin Liu, Bei Feng, Bing Xue, Bingxuan Wang, Bochao Wu, Chengda Lu, Chenggang Zhao, Chengqi Deng, Chenyu Zhang, Chong Ruan, Damai Dai, Daya Guo, Dejian Yang, Deli Chen, Dongjie Ji, Erhang Li, Fangyun Lin, Fucong Dai, Fuli Luo, Guangbo Hao, Guanting Chen, Guowei Li, H. Zhang, Han Bao, Hanwei Xu, Haocheng Wang, Haowei Zhang, Honghui Ding, Huajian Xin, Huazuo Gao, Hui Li, Hui Qu, J. L. Cai, Jian Liang, Jianzhong Guo, Jiaqi Ni, Jiashi Li, Jiawei Wang, Jin Chen, Jingchang Chen, Jingyang Yuan, Junjie Qiu, Junlong Li, Junxiao Song, Kai Dong, Kai Hu, Kaige Gao, Kang Guan, Kexin Huang, Kuai Yu, Lean Wang, Lecong Zhang, Lei Xu, Leyi Xia, Liang Zhao, Litong Wang, Liyue Zhang, Meng Li, Miaojun Wang, Mingchuan Zhang, Minghua Zhang, Minghui Tang, Mingming Li, Ning Tian, Panpan Huang, Peiyi Wang, Peng Zhang, Qiancheng Wang, Qihao Zhu, Qinyu Chen, Qiushi Du, R. J. Chen, R. L. Jin, Ruiqi Ge, Ruisong Zhang, Ruizhe Pan, Runji Wang, Runxin Xu, Ruoyu Zhang, Ruyi Chen, S. S. Li, Shanghao Lu, Shangyan Zhou, Shanhuan Chen, Shaoqing Wu, Shengfeng Ye, Shengfeng Ye, Shirong Ma, Shiyu Wang, Shuang Zhou, Shuiping Yu, Shunfeng Zhou, Shuting Pan, T. Wang, Tao Yun, Tian Pei, Tianyu Sun, W. L. Xiao, Wangding Zeng, Wanjia Zhao, Wei An, Wen Liu, Wenfeng Liang, Wenjun Gao, Wenqin Yu, Wentao Zhang, X. Q. Li, Xiangyue Jin, Xianzu Wang, Xiao Bi, Xiaodong Liu, Xiaohan Wang, Xiaojin Shen, Xiaokang Chen, Xiaokang Zhang, Xiaosha Chen, Xiaotao Nie, Xiaowen Sun, Xiaoxiang Wang, Xin Cheng, Xin Liu, Xin Xie, Xingchao Liu, Xingkai Yu, Xinnan Song, Xinxia Shan, Xinyi Zhou, Xinyu Yang, Xinyuan Li, Xuecheng Su, Xuheng Lin, Y. K. Li, Y. Q. Wang, Y. X. Wei, Y. X. Zhu, Yang Zhang, Yanhong Xu, Yanhong Xu, Yanping Huang, Yao Li, Yao Zhao, Yaofeng Sun, Yaohui Li, Yaohui Wang, Yi Yu, Yi Zheng, Yichao Zhang, Yifan Shi, Yiliang Xiong, Ying He, Ying Tang, Yishi Piao, Yisong Wang, Yixuan Tan, Yiyang Ma, Yiyuan Liu, Yongqiang Guo, Yu Wu, Yuan Ou, Yuchen Zhu, Yuduan Wang, Yue Gong, Yuheng Zou, Yujia He, Yukun Zha, Yunfan Xiong, Yunxian Ma, Yuting Yan, Yuxiang Luo, Yuxiang You, Yuxuan Liu, Yuyang Zhou, Z. F. Wu, Z. Z. Ren, Zehui Ren, Zhangli Sha, Zhe Fu, Zhean Xu, Zhen Huang, Zhen Zhang, Zhenda Xie, Zhengyan Zhang, Zhewen Hao, Zhibin Gou, Zhicheng Ma, Zhigang Yan, Zhihong Shao, Zhipeng Xu, Zhiyu Wu, Zhongyu Zhang, Zhuoshu Li, Zihui Gu, Zijia Zhu, Zijun Liu, Zilin Li, Ziwei Xie, Ziyang Song, Ziyi Gao, and Zizheng Pan. Deepseek-v3 technical report, 2025. URL <https://arxiv.org/abs/2412.19437>.

[6] Michael Andersch, Greg Palmer, Ronny Krashinsky, Nick Stam, Vishal Mehta, Gonzalo Brito, and Sridhar Ramaswamy. Nvidia hopper architecture in-depth. <https://developer.nvidia.com/blog/nvidia-hopper-architecture-in-depth/>, Mar 2022. Accessed: 2025-08-25.

[7] NVIDIA. Nvidia gb200 nvl72. <https://www.nvidia.com/en-us/data-center/gb200-nvl72/>, 2025. Accessed: 2025-08-25.

[8] NVIDIA Developer Blog. Inside nvidia blackwell ultra: The chip powering the ai factory era. <https://developer.nvidia.com/blog/inside-nvidia-blackwell-ultra-the-chip-powering-the-ai-factory-era/>, Aug 2025. Accessed: 2025-08-25.

[9] Paulius Micikevicius, Dusan Stosic, Jack J. Dongarra, Neil Burgess, Stuart Gray, Marius Cornea, Bugeun Bak, Mohammad Shoeybi, Oleksii Kuchaiev, Timothy G. Rogers, Rex Ying, Ping Tak Peter Tang, Naveen Mellempudi, Scott Leishman, Mike Scarpino, Nick S. an Mey, Stuart Mcilroy, Szymon Migacz, Yangseok Ki, Norm P. Jouppi, Cliff Young, David Patterson, and Bill Dally. FP8 formats for deep learning, 2022. URL <https://arxiv.org/abs/2209.05433>.

[10] Maxim Fishman, Brian Chmiel, Ron Banner, and Daniel Soudry. Scaling fp8 training to trillion-token llms, 2025. URL <https://arxiv.org/abs/2409.12517>.

[11] Haocheng Xi, Yuxiang Chen, Kang Zhao, Kai Jun Teh, Jianfei Chen, and Jun Zhu. Jetfire: Efficient and accurate transformer pretraining with int8 data flow and per-block quantization, 2024. URL <https://arxiv.org/abs/2403.12422>.

[12] Bita Darvish Rouhani, Nitin Garegrat, Tom Savell, Ankit More, Kyung-Nam Han, Ritchie Zhao, Mathew Hall, Jasmine Klar, Eric Chung, Yuan Yu, Michael Schulte, Ralph Wittig, Ian Bratt, Nigel Stephens, Jelena Milanovic, John Brothers, Pradeep Dubey, Marius Cornea, Alexander Heinecke, Andres Rodriguez, Martin Langhammer, Summer Deng, Maxim Naumov, Paulius Micikevicius, Michael Siu, and Colin Verrilli. Ocp microscaling formats (mx) specification, 2023. URL <https://www.opencompute.org/documents/ocp-microscaling-formats-mx-v1-0-spec-final-pdf>.

[13] Bita Darvish Rouhani, Ritchie Zhao, Ankit More, Mathew Hall, Alireza Khodamoradi, Summer Deng, Dhruv Choudhary, Marius Cornea, Eric Dellinger, Kristof Denolf, Dusan Stosic, Venmugil Elango, Maximilian Golub, Alexander Heinecke, Phil James-Roxby, Dharmesh Jani, Gaurav Kolhe, Martin Langhammer, Ada Li, Levi Melnick, Paulius Micikevicius, Maxim Naumov, Colin Verrilli, Ralph Wittig, Doug Burger, and Eric S. Chung. Microscaling data formats for deep learning, 2023. URL <https://arxiv.org/abs/2310.10537>.

[14] Asit Mishra, Dusan Stosic, Simon Layton, and Paulius Micikevicius. Recipes for pre-training llms with mxfp8, 2025. URL <https://arxiv.org/abs/2506.08027>.

[15] Kirthi Devleker and Farshad Ghodsian. Introducing nvfp4 for efficient and accurate low-precision inference. <https://developer.nvidia.com/blog/introducing-nvfp4-for-efficient-and-accurate-low-precision-inference/>, June 2025.

[16] Xiao Sun, Jungwook Choi, Chia-Yu Chen, Naigang Wang, Swagath Venkataramani, Vijayalakshmi Srinivasan, Xiaodong Cui, Wei Zhang, and Kailash Gopalakrishnan. Hybrid 8-bit floating point (hfp8) training and inference for deep neural networks. In *Advances in Neural Information Processing Systems*, volume 32, 2019. URL <https://papers.nips.cc/paper/2019/hash/65fc9fb4897a89789352e211ca2d398f-Abstract.html>.

[17] Haocheng Xi, Han Cai, Ligeng Zhu, Yao Lu, Kurt Keutzer, Jianfei Chen, and Song Han. Coat: Compressing optimizer states and activation for memory-efficient fp8 training, 2025. URL <https://arxiv.org/abs/2410.19313>.

[18] Brian Chmiel, Maxim Fishman, Ron Banner, and Daniel Soudry. Fp4 all the way: Fully quantized training of llms, 2025. URL <https://arxiv.org/abs/2505.19115>.

[19] NVIDIA, Felix Abecassis, Anjulie Agrusa, Dong Ahn, Jonah Alben, Stefania Alborghetti, Michael Andersch, Sivakumar Arayandi, Alexis BJORLIN, Aaron Blakeman, Evan Briones, Ian Buck, Bryan Catanzaro, Jinhang Choi, Mike Chrzanowski, Eric Chung, Victor Cui, Steve Dai, Bita Darvish Rouhani, Carlo del Mundo, Deena Donia, Burc Eryilmaz, Henry Estela, Abhinav Goel, Oleg Goncharov, Yugi Guvvala, Robert Hesse, Russell Hewett, Herbert Hum, Ujval Kapasi, Brucek Khailany, Mikail Khona, Nick Knight, Alex Kondratenko, Ronny Krashinsky, Ben Lanir, Simon Layton, Michael Lightstone, Daniel Lo, Paulius Micikevicius, Asit Mishra, Tim Moon, Deepak Narayanan, Chao Ni, Abhijit Paithankar, Satish Pasumarthi, Ankit Patel, Mostofa Patwary, Ashwin Poojary, Gargi Prasad, Sweta Priyadarshi, Yigong Qin, Xiaowei Ren, Oleg Rybakov, Charbel Sakr, Sanjeev Satheesh, Stas Sergienko, Pasha Shamis, Kirthi Shankar, Nishant Sharma, Mohammad Shoeybi, Michael Siu, Misha Smelyanskiy, Darko Stosic, Dusan Stosic, Bor-Yiing Su, Frank Sun, Nima Tajbakhsh, Shelby Thomas, Przemek Tredak, Evgeny Tsykunov, Gandhi Vaithilingam, Aditya Vavre, Rangharajan Venkatesan, Roger Waleffe, Qiyu Wan, Hexin Wang, Mengdi Wang, Lizzie Wei, Hao Wu, Evan Wu, Keith Wyss, Ning Xu, Jinze Xue, Charlene Yang, Yujia Zhai, Ruoxi Zhang, Jingyang Zhu, and Zhongbo Zhu. Pretraining large language models with nvfp4, 2025. URL <https://arxiv.org/abs/2509.25149>.

[20] Coleman Hooper, Charbel Sakr, Ben Keller, Rangharajan Venkatesan, Kurt Keutzer, Sophia Shao, and Brucek Khailany. Fgmp: Fine-grained mixed-precision weight and activation quantization for hardware-accelerated llm inference, 2025. URL <https://arxiv.org/abs/2504.14152>.

[21] NVIDIA. Nemotron-3-8b-base-4k. NVIDIA NGC Catalog, November 2024. URL <https://catalog.ngc.nvidia.com/orgs/nvidia/teams/nemo/models/nemotron-3-8b-base-4k>. Accessed: 2025-09-19.

[22] Mohammad Shoeybi, Mostofa Patwary, Raul Puri, Patrick LeGresley, Jared Casper, and Bryan Catanzaro. Megatron-lm: Training multi-billion parameter language models using model parallelism, 2020. URL <https://arxiv.org/abs/1909.08053>.

[23] Bo Adler, Niket Agarwal, Ashwath Aithal, Dong H. Anh, Pallab Bhattacharya, Annika Brundyn, Jared Casper, Bryan Catanzaro, Sharon Clay, Jonathan Cohen, Sirshak Das, Ayush Dattagupta, Olivier Delalleau, Leon Derczynski, Yi Dong, Daniel Egert, Ellie Evans, Aleksander Ficek, Denys Fridman, Shaona Ghosh, Boris Ginsburg, Igor

Gitman, Tomasz Grzegorzek, Robert Hero, Jining Huang, Vibhu Jawa, Joseph Jennings, Aastha Jhunjhunwala, John Kamalu, Sadaf Khan, Oleksii Kuchaiev, Patrick LeGresley, Hui Li, Jiwei Liu, Zihan Liu, Eileen Long, Ameya Sunil Mahabaleshwarkar, Somshubra Majumdar, James Maki, Miguel Martinez, Maer Rodrigues de Melo, Ivan Moshkov, Deepak Narayanan, Sean Narendhiran, Jesus Navarro, Phong Nguyen, Osvald Nitski, Vahid Noroozi, Guruprasad Nutheti, Christopher Parisien, Jupinder Parmar, Mostofa Patwary, Krzysztof Pawelec, Wei Ping, Shrimai Prabhumoye, Rajarshi Roy, Trisha Saar, Vasanth Rao Naik Sabavat, Sanjeev Satheesh, Jane Polak Scowcroft, Jason Sewall, Pavel Shamis, Gerald Shen, Mohammad Shoeybi, Dave Sizer, Misha Smelyanskiy, Felipe Soares, Makesh Narsimhan Sreedhar, Dan Su, Sandeep Subramanian, Shengyang Sun, Shubham Toshniwal, Hao Wang, Zhilin Wang, Jiaxuan You, Jiaqi Zeng, Jimmy Zhang, Jing Zhang, Vivienne Zhang, Yian Zhang, and Chen Zhu. Nemotron-4 340b technical report, 2024. URL <https://arxiv.org/abs/2406.11704>.

[24] Aaron Blakeman, Aarti Basant, Abhinav Khattar, Adithya Renduchintala, Akhiad Bercovich, Aleksander Ficek, Alexis BJORLIN, Ali Taghibakhsh, Amala Sanjay Deshmukh, Ameya Sunil Mahabaleshwarkar, Andrew Tao, Anna Shors, Ashwath Aithal, Ashwin Poojary, Ayush Dattagupta, Balaram Buddharaju, Bobby Chen, Boris Ginsburg, Boxin Wang, Brandon Norick, Brian Butterfield, Bryan Catanzaro, Carlo del Mundo, Chengyu Dong, Christine Harvey, Christopher Parisien, Dan Su, Daniel Korzekwa, Danny Yin, Daria Gitman, David Mosallanezhad, Deepak Narayanan, Denys Fridman, Dima Rekesh, Ding Ma, Dmytro Pykhtar, Dong Ahn, Duncan Riach, Dusan Stosic, Eileen Long, Elad Segal, Ellie Evans, Eric Chung, Erick Galinkin, Evelina Bakhturina, Ewa Dobrowolska, Fei Jia, Fuxiao Liu, Gargi Prasad, Gerald Shen, Guilin Liu, Guo Chen, Haifeng Qian, Helen Ngo, Hongbin Liu, Hui Li, Igor Gitman, Ilia Karmanov, Ivan Moshkov, Izik Golan, Jan Kautz, Jane Polak Scowcroft, Jared Casper, Jarno Seppanen, Jason Lu, Jason Sewall, Jiaqi Zeng, Jiaxuan You, Jimmy Zhang, Jing Zhang, Jining Huang, Jinze Xue, Jocelyn Huang, Joey Conway, John Kamalu, Jon Barker, Jonathan Cohen, Joseph Jennings, Jupinder Parmar, Karan Sapra, Kari Briski, Kateryna Chumachenko, Katherine Luna, Keshav Santhanam, Kezhi Kong, Kirthi Sivamani, Krzysztof Pawelec, Kumar Anik, Kunlun Li, Lawrence McAfee, Leon Derczynski, Lindsey Pavao, Luis Vega, Lukas Voegtle, Maciej Bala, Maer Rodrigues de Melo, Makesh Narsimhan Sreedhar, Marcin Chochowski, Markus Kliegl, Marta Stepniewska-Dziubinska, Matthieu Le, Matvei Novikov, Mehrzad Samadi, Michael Andersch, Michael Evans, Miguel Martinez, Mike Chrzanowski, Mike Ranzinger, Mikolaj Blaz, Misha Smelyanskiy, Mohamed Fawzy, Mohammad Shoeybi, Mostofa Patwary, Nayeon Lee, Nima Tajbakhsh, Ning Xu, Oleg Rybakov, Oleksii Kuchaiev, Olivier Delalleau, Osvald Nitski, Parth Chadha, Pasha Shamis, Paulius Micikevicius, Pavlo Molchanov, Peter Dykas, Philipp Fischer, Pierre-Yves Aquilanti, Piotr Bialecki, Prasoon Varshney, Pritam Gundecha, Przemek Tredak, Rabeeh Karimi, Rahul Kandu, Ran El-Yaniv, Raviraj Joshi, Roger Waleffe, Ruoxi Zhang, Sabrina Kavanaugh, Sahil Jain, Samuel Kriman, Sangkug Lym, Sanjeev Satheesh, Saurav Muralidharan, Sean Narendhiran, Selvaraj Anandaraj, Seonmyeong Bak, Sergey Kashirsky, Seungju Han, Shantanu Acharya, Shaona Ghosh, Sharath Turuvekere Sreenivas, Sharon Clay, Shelby Thomas, Shrimai Prabhumoye, Shubham Pachori, Shubham Toshniwal, Shyamala Prayaga, Siddhartha Jain, Sirshak Das, Slawek Kierat, Somshubra Majumdar, Song Han, Soumye Singhal, Sriharsha Niverty, Stefania Alborghetti, Suseella Panguluri, Swetha Bhendigeri, Syeda Nahida Akter, Szymon Migacz, Tal Shiri, Terry Kong, Timo Roman, Tomer Ronen, Trisha Saar, Tugrul Konuk, Tuomas Rintamaki, Tyler Poon, Ushnish De, Vahid Noroozi, Varun Singh, Vijay Korthikanti, Vitaly Kurin, Wasi Uddin Ahmad, Wei Du, Wei Ping, Wenliang Dai, Wonmin Byeon, Xiaowei Ren, Yao Xu, Yejin Choi, Yian Zhang, Ying Lin, Yoshi Suhara, Zhiding Yu, Zhiqi Li, Zhiyu Li, Zhongbo Zhu, Zhuolin Yang, and Zijia Chen. Nemotron-h: A family of accurate and efficient hybrid mamba-transformer models, 2025. URL <https://arxiv.org/abs/2504.03624>.